

The CaFe Project: Optical Fe II and Near-Infrared Ca II triplet emission in active galaxies (I) Photoionization modelling

SWAYAMTRUPTA PANDA,^{1,2} MARY LOLI MARTÍNEZ-ALDAMA,¹ MURILO MARINELLO,³ BOŻENA CZERNY,¹
PAOLA MARZIANI,⁴ AND DEBORAH DULTZIN⁵

¹*Center for Theoretical Physics, Polish Academy of Sciences, Al. Lotników 32/46, 02-668 Warsaw, Poland*

²*Nicolaus Copernicus Astronomical Center, Polish Academy of Sciences, ul. Bartycka 18, 00-716 Warsaw, Poland*

³*Laboratório Nacional de Astrofísica, R. dos Estados Unidos, 154 - Nações, Itajubá - MG, 37504-364, Brazil*

⁴*INAF-Astronomical Observatory of Padova, Vicolo dell'Osservatorio, 5, 35122 Padova PD, Italy*

⁵*Universidad Nacional Autónoma de México Instituto de Astronomía: Ciudad de México, Distrito Federal, MX 04510, Mexico*

(Received September 8, 2020; Revised September 8, 2020; Accepted September 8, 2020)

Submitted to ApJ

ABSTRACT

Optical Fe II emission is a strong feature in quasar spectra originating in the broad-line region (BLR). The difficulty in understanding the complex Fe II pseudo-continuum has led us to search for other reliable, simpler ionic species such as Ca II. In this first part of the series, we confirm the strong correlation between the strengths of two emission features, the optical Fe II and the NIR Ca II, both from observations and photoionization modelling. With the inclusion of an up-to-date compilation of observations with both optical Fe II and NIR Ca II measurements, we span a wider and more extended parameter space and confirm the common origin of these two spectral features with our photoionization models using CLOUDY. Taking into account the effect of dust into our modelling, we constrain the BLR parameter space (primarily, in terms of the ionization parameter and local cloud density) as a function of the strengths of Fe II and Ca II emission.

Keywords: galaxies: active, quasars: emission lines; accretion disks; radiative transfer; scaling relations

1. INTRODUCTION

Fe II emission in active galactic nuclei (AGNs) covers a wide range of energy bands – typically spreading from the ultraviolet (UV) to the near-infrared region (NIR) – and contains numerous multiplets. These multiplets form a pseudo-continuum owing to the blending of over 344,000 transitions (Bruhweiler & Verner 2008). Understanding the origin of the Fe emission in AGNs is a major challenge and is important for a number of reasons as summarized in Marinello et al. (2016). One of the primary reasons is its role as a strong contaminant due to the large number of lines. This may lead to an inaccurate estimate of parameters for lines from other ionic species and hence to an improper description of

the physical conditions in the broad-line region (BLR). The Fe II pseudo-continuum requires proper modelling taking into account the radiative mechanisms responsible for its emission and the chemical composition of the BLR clouds (Verner et al. 1999; Bruhweiler & Verner 2008; Kovačević et al. 2010; Panda et al. 2018).

Boroson & Green (1992) provided one of the first Fe II templates that has been ubiquitously used to subtract the contamination due to Fe II in the optical band of quasar spectra. The Fe II template has been obtained in a very simple way by removing lines that are not Fe II in the PG 0050+124 (I Zw 1) spectrum. The result of their procedure was a spectrum representing only permitted Fe II emission in I Zw 1 (after removing Balmer lines, [OIII] $\lambda\lambda$ 4959, 5007 lines, [NII] λ 5755, blend of Na I D and He I λ 5876, two intense [Fe II] lines at λ 5158Å and λ 5273Å). The use of I Zw 1 was motivated by the fact that emission lines in this source were very narrow

and their subtraction did not affect much a broad wavelength range.

The term ‘‘Fe II pseudo-continuum’’ drew importance after the seminal work of Verner et al. (1999) which developed a theoretical model for the Fe II emission taking into account transition probabilities and collision strengths from the up-to-date atomic data available at that time (see also Sigut & Pradhan 2003). Their Fe II atom model included 371 levels (up to 11.6 eV) and predicted intensities of 68,635 lines. Later works have tested the Fe II templates procedure by semi-empirical methods – in the optical (Véron-Cetty et al. 2004; Kovačević et al. 2010) and in the NIR (Garcia-Rissmann et al. 2012), as well as from the purely observational spectral fitting in the UV (Vestergaard & Wilkes 2001).

Fe II emission also bears extreme importance in the context of the main sequence of quasars. Several noteworthy works have established the prominence of the strength of the optical Fe II emission (4434-4684 Å) with respect to the *broad* H β line width (henceforth R_{FeII}) and it’s relevance to the Eigenvector 1 sequence primarily linked to the Eddington ratio (Boroson & Green 1992; Sulentic et al. 2000b, 2001; Shen & Ho 2014; Marziani et al. 2018a). Recent studies have addressed the importance of the Fe II emission and its connection with the Eddington ratio, the black hole mass, cloud density, metallicity and turbulence (Panda et al. 2018), as well as with the shape of the ionizing continuum (Panda et al. 2019a), and including the effect of the orientation of the disk plane with respect to the observer (Panda et al. 2019b, 2020).

The difficulty in understanding the Fe II emission has motivated us to search of other reliable, simpler ionic species such as Ca II and O I (Martínez-Aldama et al. 2015a, and references therein) which would originate from the same part of the BLR and could play a similar role in quasar main sequence studies. Here, by Ca II emission we refer to the Ca II IR triplet (CaT), consisting of lines at $\lambda 8498\text{\AA}$, $\lambda 8542\text{\AA}$ and $\lambda 8662\text{\AA}$. Photoionization models performed by Joly (1989) have shown that the relation between the ratios CaT/H β and R_{FeII} provides evidence for a common origin for the NIR CaT and optical Fe II. CaT/H β increases at high density and low temperature as does R_{FeII} (Joly 1987; Dultzin-Hacyan et al. 1999). Persson (1988) conducted the first survey for Ca II emission in 40 AGNs. Data from Persson (1988) and photoionization calculations from Joly (1989) found that CaT is emitted by gas at low temperature (8000 K), high density ($> 10^{11} \text{ cm}^{-3}$) similar to optical Fe II. Matsuoka et al. (2007, 2008) computed photoionization models using the O I $\lambda 8446$ and $\lambda 11287$ lines and CaT, and found that a high density ($\sim 10^{11}$

cm^{-3}) and low ionization parameter ($\log U \sim -2.5$) are needed to reproduce flux ratios consistent with the physical conditions expected for optical Fe II emission.

A recent study by Martínez-Aldama et al. (2015a) found the best fit relation for the CaT strength (or CaT/H β) to that of R_{FeII} is given by the following relation:

$$\log \left(\frac{\text{CaT}}{\text{H}\beta} \right) = (1.33 \pm 0.23) \log \left(\frac{\text{Fe II}}{\text{H}\beta} \right) - (0.63 \pm 0.07) \quad (1)$$

In this paper we reaffirm the relation between the ratios CaT/H β (hereafter, R_{CaT}) and R_{FeII} using photoionization modelling and comparing with an up-to-date compilation of sources, and identify the physical conditions characterizing the emitting zones in terms of two key parameters – *ionization parameter* (U) and *local cloud density* (n_{H}). Section 2.1 presents the sample compiled from prior observational studies, and Section 2.2 describes the CLOUDY (Ferland et al. 2017) photoionization modelling setup, including a dust prescription applied in the post-photoionization stage of the computations. We analyse the results from the modelling and compare them with the results from the observations in Section 3. We discuss certain relevant issues in Section 4 and summarize our results in Section 5 with possible extensions in the future. Throughout this work, we assume a standard cosmological model with $\Omega_{\Lambda} = 0.7$, $\Omega_m = 0.3$, and $H_0 = 70 \text{ km s}^{-1} \text{ Mpc}^{-1}$.

2. METHODS

2.1. Observational data

The studies of the NIR calcium triplet properties have by now some history. The first observations of this ion were published in the late-1990s (Persson 1988), and soon after some theoretical analysis (Joly 1989; Ferland & Persson 1989) followed. Up to now, 75 CaT measurements are available in the literature (Persson 1988; Matsuoka et al. 2005; Riffel et al. 2006; Matsuoka et al. 2007; Martínez-Aldama et al. 2015a,b; Marinello et al. 2016, 2020). However, not all of them are reliable. Observations of CaT pre-dating NIR spectrographs on large aperture telescopes relied on optical observations. Although it is possible to observe 0.8–0.9 μm region, where the CaT is located, with standard optical telescopes the observations are limited to low redshift sources. Besides, since the CaT equivalent width is considerably lower than for the hydrogen lines, very long exposure times are required to achieve a good signal to noise measurement of those lines. This restricts observation to bright sources and implies strong contamination of OH telluric lines present in this region. Moreover, the host galaxy (particularly the calcium absorption lines) can be

present and suppress the contribution of the CaT emission. Since NIR spectrographs became an option, the number of AGNs with reliable CaT measurements has increased, although no large survey has been carried out yet.

Optical measurements for $H\beta$ and R_{FeII} are required in our analysis, in addition to reliable measurements of the CaT. As a consequence, we were able to select 58 objects. The full sample includes sources with $42.5 < \log L_{5100} < 46.8$ at $0.01 < z < 1.68$. A description of the sample and the relevant measurements for the present analysis are shown in Table 1. The measurements are collected from the original works described in detail in the following sub-sections. Persson (1988) and Marinello et al. (2016) samples have a coincidence in 5 sources, and we use both measurements. These five objects are marked in Table 1.

2.1.1. Persson (1988) sample

The Persson (1988) study was the first analysis devoted to the Ca II triplet measurements. Due to the selection criteria of the sample, the majority of the sources are mostly catalogued as NLS1 objects. Since CaT and Fe II intensities are correlated, only strong Fe II emitters were selected for ensuring the presence of the CaT. Also, in order to avoid the blending between O I $\lambda 8446$ and the first two lines of the Ca II triplet at 8498\AA and 8542\AA , only narrow $H\beta$ profiles were selected. These criteria introduce a selection effect in the sample. The original sample included 40 sources with $-27.0 < M_V < -20.0$ at $0.009 < z < 0.159$. Persson (1988) divided the sample into four categories by a visual inspection considering the quality of the observation, the CaT strength and the presence of the host galaxy contamination. The first category includes objects without any doubt of the presence of CaT emission; however, some of these objects show a central dip in the CaT emission lines indicating the contribution from the host galaxy. The rest of the categories include sources with moderate Ca II emission or a clear host galaxy contamination. Due to the limitation of the signal-to-noise ratio (S/N) of the sample, the decomposition of the host galaxy was not performed, and, Persson in his paper excluded 15 of the most contaminated sources. For the remaining objects, the CaT measurement was still possible, although the reliability of the measurement had to be assessed on a case-by-case basis. We have considered the remaining 25 objects with a CaT measurement reported, where at least five do not show a dip in the CaT emission lines suggesting no contamination from a stellar continuum. Since some measurements might be problematic and others are reported as upper limits, we include the

corresponding information in Table 1, where we also report the identification of the source, redshift, R_{FeII} , and R_{CaT} intensity ratio for the sources considered in this work.

2.1.2. Martínez-Aldama et al. (2015a,b) sample

With the purpose of increasing the number of objects, enlarge the redshift and luminosity range covered by the Persson (1988), Martínez-Aldama et al. (2015a,b) observed a total 21 QSO with the Very Large Telescope (VLT) using the Infrared Spectrometer And Array Camera (ISAAC¹). The selection criteria, data reduction, and analysis are the same in the two papers of Martínez-Aldama and collaborators. Since the CaT has a low equivalent width compared to the equivalent width of $H\beta$ (Joly 1989), they selected the brightest (and hence most luminous, $-29 < M_V < -26$) sources of the intermediate redshift QSO sample ($0.85 < z < 1.68$) which were later studied by Sulentic et al. (2017). This increases the probability to observe a high signal-to-noise (S/N) spectrum in the NIR, which is required for a careful analysis. Therefore, this sample is not as biased in terms of Fe II intensity as Persson (1988)'s. The majority of the sources in this sample show broad profiles, which differentiate them from the Persson and Marinello samples. While in these samples (Persson 1988; Marinello et al. 2016, 2020, the latter are described in the following subsection.) the CaT can be resolved individually, in Martínez-Aldama et al. sample the CaT is blended with the O I $\lambda 8446$.

On the other hand, since that sample is of high luminosity ($L_{\text{bol}} \sim 10^{47} \text{ erg s}^{-1}$), it is expected that the host galaxy contamination should be much smaller. In order to estimate and subtract the host galaxy contribution, they obtained the specific flux at 9000 \AA from the stellar population synthesis models, and then estimated the host mass assuming the $M_{\text{bulge}}/M_{\text{BH}}$ ratio (Merloni et al. 2010; Magorrian et al. 1998) appropriate for the redshift of each quasar. They found that in the majority of the sample the contribution of the host is $\lesssim 10\%$, except in the quasar HE 2202-2557 where it has a contribution of $\sim 50\%$ with respect to the total luminosity. In fact, before the host galaxy subtraction, the absorption features could be observed by eye in this object. Hence, the host galaxy contribution was only subtracted in HE 2202-2557.

2.1.3. Marinello et al. (2016) sample + PHL1092

The original sample from Marinello et al. (2016) consists of 25 AGNs which were selected primarily from the

¹ ISAAC was decommissioned in 2013.

list of Joly (1991). The 25 AGN spectra were taken from the AGN NIR atlas presented by Riffel et al. (2016) and complemented with the spectra observed by Rodríguez-Ardila et al. (2002). Their sample was observed with SpeX (Rayner et al. 2003) at the 3 m *NASA Infrared Telescope Facility* (IRTF), a NIR spectrograph used in the cross-dispersed mode to observe simultaneously 0.7–2.4 μm , with a resolution $R \sim 1300$. The additional selection criteria imposed in the NIR sample selection were: (1) the target K-band magnitude brighter than 12 to balance between a good S/N and exposure time; and (2) FWHM of the broad $H\beta$ component less than 3000 km s^{-1} . The latter limitation was introduced to ensure that severe blending from Fe II lines with adjacent permitted and forbidden lines is avoided. Among these 25 AGNs, only 13 had Ca II $\lambda 8662$ fluxes and FWHMs available, and among these 13, only 10 had concomitant R_{FeII} estimates. Hence, we consider these 10 sources in our sample.

Besides those 10 AGNs from Marinello et al. (2016), we add to our sample an extreme-strong Fe II emitter, PHL 1092, from Marinello et al. (2020). PHL 1092 was the strongest Fe II emitter reported by Joly (1991), with a $R_{\text{FeII}}=6.2$. Marinello et al. (2020) presented a panchromatic analysis of the physical properties of this AGN using a combined spectrum of HST/STIS (in the ultraviolet), SOAR/Goodman (in the optical), and GNIRS/Gemini (in the NIR), covering a wavelength range of 0.1–1.6 μm . The high S/N and resolution from Goodman spectrograph allowed them to re-estimate R_{FeII} , obtaining a value of 2.58, which still places PHL 1092 among the strongest Fe II emitters observed.

For 4 out of 10 sources from Marinello et al. (2016) sample – 1H1934, Mrk335, Mrk493, Tons180; and for PHL1092, we notice that the emission line profiles were better represented by a Lorentzian function rather a Gaussian, as originally assumed by the authors. These sources are known narrow line Seyfert 1 galaxies, and part of the Population A (Marziani et al. 2001), where broad lines usually have a Lorentzian-shaped profile. We re-fit the Ca II, $H\beta$, and O I lines, and re-estimate the Fe II intensity for these sources. Note that since these lines are blended – either with its own narrow component (in the case of $H\beta$), or with other broad lines (for Ca II $\lambda\lambda 8496, 8542$ and O I), this re-analysis results in higher fluxes of these lines, on average by $\sim 15\%$ for the 5 sources.

There is no report of host galaxy stellar population (SP) in the sample of Marinello et al. (2016) and PHL 1092. Their sample consists of strong emission line AGNs, with low or no SP signatures in the spectra. The

two main SP features in the NIR spectrum are the CO bands redwards of 2.3 μm and the Ca II triplet absorption around 0.8 μm (Riffel et al. 2006). Since their sample is dominated by emission lines, the absorption around Ca II triplet is not visible in the spectra. Moreover, the redshifts of the sources do not allow a reliable measurement of the CO bands, since it is outside the wavelength coverage of the instrument. For these reasons, Marinello et al. (2016) considered an error of up to 10% due to the host galaxy on the continua in their measurements.

2.2. Photoionization modelling setup

We perform a suite of CLOUDY models aimed at understanding the physical conditions in the BLR medium leading to efficient production of CaT and to test the connection between CaT and Fe II emissivities. Our simulated grid was created by varying the cloud particle density, $10^5 \leq n_{\text{H}} \leq 10^{13}$ (cm^{-3}), and the ionization parameter, $-7 \leq \log U \leq 0$. The modelling setup applies a single cloud model, but assumes a grid of ionization parameters and cloud densities, which allows to reproduce a range of BLR radii for a fixed number of ionizing photons emanating from the central region. We do not apply the more complex *Locally Optimized Cloud* (LOC) prescription (Baldwin et al. 1995) which requires integration of the cloud emissivity over a range of densities and radii that are assumed to have power law distributions for each model. Such a model has more parameters since, apart from the power law slopes, the results do depend on the adopted outer radius of the BLR and the maximum allowed cloud density (see e.g. Goad & Korista 2015). The single cloud model, although simplistic in its approach, has proved to be quite successful in estimating the optical Fe II emission line strengths as has been verified in our previous works (Panda et al. 2017, 2018, 2019a,b, 2020). It was also used by Negrete et al. (2013) where they were able to reproduce three line ratios without restoring to LOC model. There is a theoretical argument in favor of the universal local density of the BLR clouds which is based on radiation pressure confinement (Baskin & Laor 2018a). The remaining parameters are the cloud column density (N_{H}) for which we assume a value of 10^{24} cm^{-2} in our Base Model, motivated by our past studies (Panda et al. 2017, 2018, 2019a). Such a column density is sufficiently large to give low ionization lines while still keeping the medium optically thin. This allows us to neglect the additional effect from the electron scattering that starts to play a role for media that are optically thick ($\tau \gtrsim 10$). In our Base Model we also fix chemical composition of the medium at solar abundance (Z_{\odot}) which are estimated using the *GASS10* module (Grevesse et al. 2010). The

effect of the change in metallicity is addressed in Section 3.3.1 accounting for a sub-solar case ($Z = 0.2Z_{\odot}$) and a super-solar case ($Z = 5Z_{\odot}$). We also test the effect of the change in column density to higher values, such as, $10^{24.5} \text{ cm}^{-2}$ and 10^{25} cm^{-2} , which is addressed in Section 3.3.2. Indeed, one expects a broad range of column densities to be present in the BLR, yet, this value of the N_H quite consistently reproduces the observed line emission, especially in the case of the optical and UV Fe II as shown in Bruhweiler & Verner (2008). We utilize the spectral energy distribution (SED) for the nearby ($z=0.061$) Narrow Line Seyfert 1 (NLS1), I Zw 1². We assume that the observed SED is also the one seen by the BLR gas. The parameters R_{FeII} and R_{CaT} are extracted from these simulations³, where R_{FeII} is the Fe II intensities integrated between 4434-4684 Å and normalized by the broad H β $\lambda 4861\text{Å}$ intensity, and similarly, R_{CaT} is the sum of the intensities for the Ca II triplet at $\lambda 8498\text{Å}$, $\lambda 8542\text{Å}$ and $\lambda 8662\text{Å}$ normalized by the same broad H β intensity.

2.3. Inclusion of dust sublimation

We assume that the BLR outer radius is given by the inner radius of the dusty/molecular torus (Netzer & Laor 1993) which constrains the available parameter space. Our approach assumes dustless clouds in the BLR, and the dust sublimation temperature limits the considered size of the BLR. As shown in Kishimoto et al. (2007) (adopted from Barvainis 1987), the dust sublimation radius depends collectively on the source luminosity (L_{UV} , coming from the accretion disk), the sublimation temperature of the dust (T_{sub}), and the dust grain size (a),

$$R_{\text{sub}} [\text{pc}] = 1.3 \left(\frac{L_{\text{UV}}}{10^{46}} \right)^{0.5} \left(\frac{T_{\text{sub}}}{1500 \text{ K}} \right)^{-2.8} \left(\frac{a}{0.05 \mu\text{m}} \right)^{-0.5} \quad (2)$$

The prescription from Nenkova et al. (2008) which we apply to estimate the dust sublimation radius in this paper assumes, for simplicity, a dust temperature $T_{\text{sub}} = 1500 \text{ K}$, which has been found consistent with the adopted mixture of the silicate and graphite dust grains. The actual form of their Equation 1 is given as:

$$R_{\text{sub}} [\text{pc}] = 0.4 \left(\frac{L_{\text{UV}}}{10^{45}} \right)^{0.5} \left(\frac{T_{\text{sub}}}{1500 \text{ K}} \right)^{-2.6} \quad (3)$$

² The I Zw 1 ionizing continuum shape is obtained from Vizier photometric viewer.

³ The CLOUDY output files for each model (inclusive of the SED shape and a sample input) are hosted on our GitHub repository: <https://github.com/Swayamtrupta/CaT-FeII-emission>.

This has a slightly different form than Equation 2 which is originally derived in Barvainis (1987). Nenkova et al. (2008) solves the radiative transfer problem for smooth density distributions which does not involve separately the size of the dust grains or their volume density, and hence the grain size parameter is dropped (for $a = 0.05 \mu\text{m}$). This is the origin for the slightly steeper exponent for the dust-temperature part in their relation compared to Barvainis (1987). Upon simplification, the prescription from Nenkova et al. (2008) has a form: $R_{\text{sub}} = 0.4 (L_{\text{UV}}/10^{45})^{0.5}$ [parsecs], where, R_{sub} is the sublimation radius computed from the source luminosity that is consistent for a characteristic dust temperature. The sublimation radius is estimated using the integrated optical-UV luminosity for I Zw 1. This optical-UV luminosity is the manifestation for an accretion disk emission and can be used as an approximate of the source's bolometric luminosity. The bolometric luminosity of I Zw 1 is $L_{\text{bol}} \sim 4.32 \times 10^{45} \text{ erg s}^{-1}$. This is obtained by applying the bolometric correction prescription from Netzer (2019) to I Zw 1's optical monochromatic luminosity, $L_{5100} \sim 3.48 \times 10^{44} \text{ erg s}^{-1}$ (Persson 1988). This uniquely sets the dust sublimation radius at $\sim 0.83\text{pc}$ ($= 2.56 \times 10^{18} \text{ cm}$). Projecting this sublimation radius on the $\log U - \log n_H$ plane allows us to recover the non-dusty region that well represents the physical parameter space consistent with the emission from the BLR (see Fig. 1). This dust-filtering is applied to the models in a post-photoionization stage.

3. ANALYSIS AND RESULTS

3.1. Physical conditions in the CaT and Fe II emitting regions

We used our basic simulation grid to compare the parameter ranges of density and ionization parameter corresponding to the most efficient production of CaT and Fe II. The left panel of Figure 1 shows the $\log U - \log n_H$ plane as a function of the ratio R_{FeII} ; the right panel shows the corresponding distribution for R_{CaT} . The red line limits the region to the dustless BLR⁴. Clearly, the zones are very similar, although the CaT emission is seemingly more extended than the one for Fe II – stretching to densities $\lesssim 10^{9.5} \text{ cm}^{-3}$ albeit at very high ionization ($\log U \gtrsim -1$). Also, the maximum of the emission for CaT is concentrated in a region which has relatively high densities ($10^{11.5} \lesssim n_H \lesssim 10^{12.25} \text{ cm}^{-3}$) but requires

⁴ Note: the limits on the colorbar are different for the left and right panels. This is done to emphasize the zone of maximum emission in both these cases. As the two ratios are normalized with respect to the intensity of H β , we effectively map the emitting regions for the Fe II and CaT, respectively.

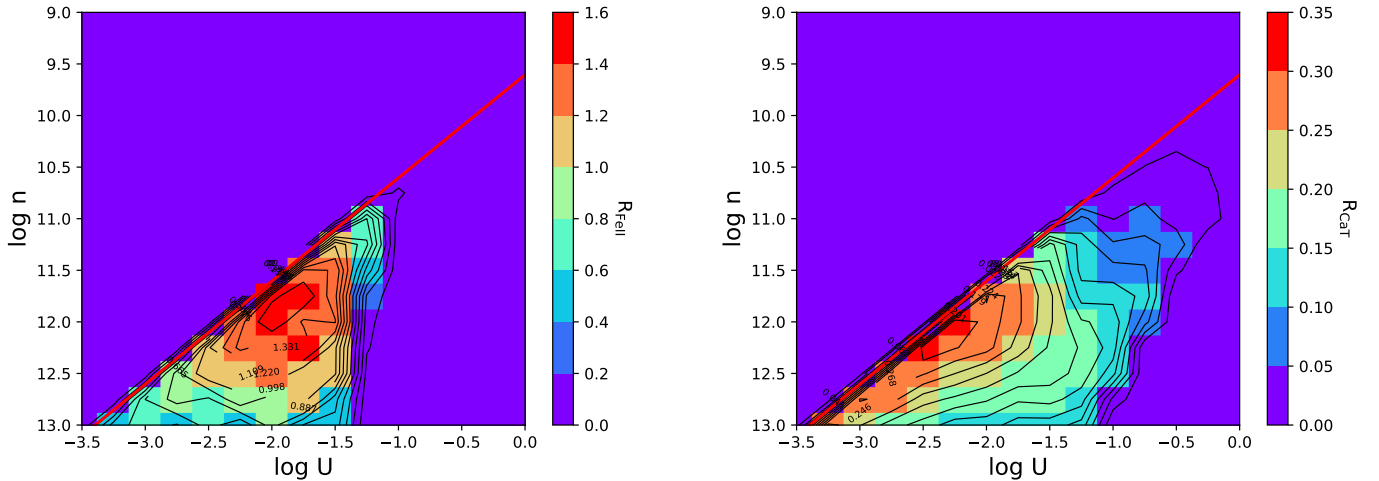


Figure 1. 2D histograms showing $\log U - \log n_{\text{H}}$ for (a) R_{FeII} ; and (b) R_{CaT} ; for the base model, i.e. at $Z = Z_{\odot}$, $N_{\text{H}} = 10^{24} \text{ cm}^{-2}$. The solid red line denotes the dust sublimation radius ($R_{\text{sub}} = 0.83 \text{ pc}$) considering [Nenkova et al. \(2008\)](#) prescription. The black contours also represent the R_{FeII} and R_{CaT} emission, respectively.

lower ionization parameters ($-2.5 \lesssim \log U \lesssim -2.0$) than Fe II. Furthermore, we find that the maximum R_{FeII} is by a factor ~ 4.5 higher than the corresponding R_{CaT} maximum.

A related fundamental question in this context is – How to confirm whether the Fe II emission is confined to the BLR? Previous studies ([Panda et al. 2018](#), and references therein) have been able to quantify the Fe II emission in the BLR and compare it to the values obtained from observations – using the DR7 quasar catalogue ([Shen et al. 2011](#)). They further constrained the location of the emitting region for the species by studying their emissivity profiles with respect to $\text{H}\beta$. The emissivity profiles provide a confirmation of the results obtained from the time-lag measurements of Fe II based on reverberation mapping of selected AGNs ([Barth et al. 2013](#); [Hu et al. 2015](#)). To confirm this in the context of the current study, we procure a sample of reverberation-mapped selected AGNs from [Negrete et al. \(2013\)](#) wherein the authors had estimated the size of the BLR using the photoionization method by employing diagnostic line ratios in the UV. In addition to confirming the BLR size which were found in good agreement to the reverberation-mapped estimates, the authors were able to estimate the ionization parameter and the density for the 13 sources. Figure 2 shows these estimates in the $\log U - \log n_{\text{H}}$ space overlaid on top of our photoionization model setup for both R_{FeII} and R_{CaT} cases. This further confirms that both these emitting regions are present in the BLR considered in this work. The observational points from that sample may imply that the actual parameter range in BLR is narrower than adopted in our simulations, but the sources populate the region of the highest emissivity.

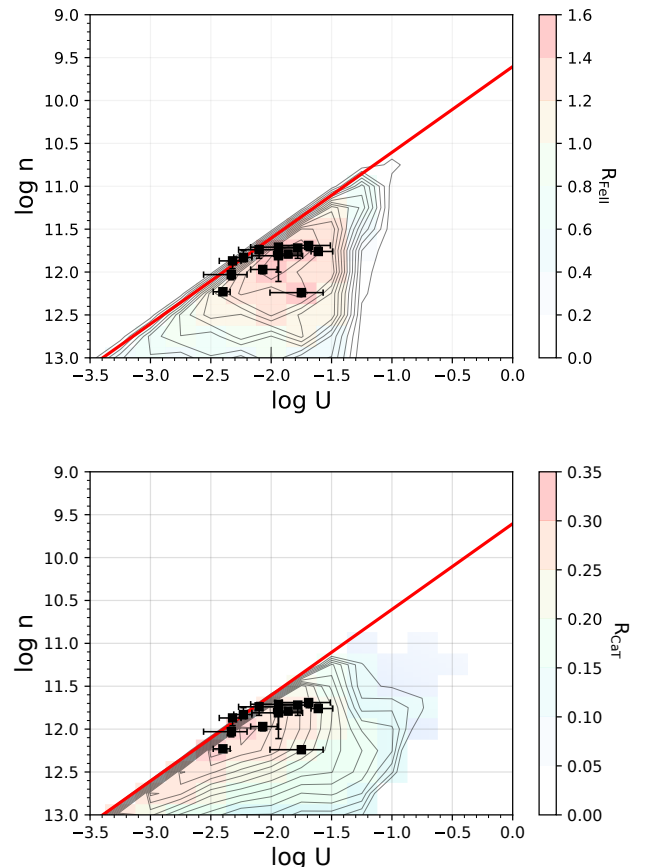


Figure 2. $\log U - \log n_{\text{H}}$ estimates for 13 *reverberation-mapped* AGNs from [Negrete et al. \(2013\)](#). Our photoionization setup color-coded with R_{FeII} (upper-panel) and with R_{CaT} (lower-panel) is shown in the background (identical to Figure 1).

3.2. R_{CaT} vs. R_{FeII} : observations

Figure 3 shows the correlation between the R_{CaT} and R_{FeII} both from observations and from our photoionization modelling (Base model). For the observed sample the correlation between the R_{CaT} and R_{FeII} is strong and significant, with the correlation coefficient $r \approx 0.737$, and a p-value = 4.33×10^{-11} . The best-fit relation for the full sample from observations is:

$$\log\left(\frac{\text{CaT}}{\text{H}\beta}\right) \approx (0.974 \pm 0.119) \log\left(\frac{\text{Fe II}}{\text{H}\beta}\right) - (0.657 \pm 0.041) \quad (4)$$

which has a slope consistent with simple proportionality between the two quantities, with more scatter in the lower range. The best fit slope reported by [Martínez-Aldama et al. \(2015a\)](#) was considerably higher (1.33 vs. 0.974 in this paper) but the two values are still consistent within a 3σ limit. The change in the slope resulted from inclusion of more data, particularly half of [Marinello et al. \(2016\)](#) sample populate the bottom-right part of the relation resulting in a slightly shallow trend. In fact, this sample includes objects with the highest R_{FeII} and R_{CaT} values, which were underrepresented in the previous sample of ([Martínez-Aldama et al. 2015a,b](#)). In an upcoming paper, we will explore the different kinds of AGN included in our sample considering the 4DE1 scheme ([Sulentic et al. 2000a](#); [Marziani et al. 2018b](#)).

We decided to keep also the results from the older observations ([Persson 1988](#)) which were re-observed and re-analysed in [Marinello et al. \(2016\)](#). The more recent observations of the five sources that are in common show a larger R_{FeII} and R_{CaT} . These differences can be caused by different methods of fitting the Fe II bump and the $\text{H}\beta$ profile. For instance, the work of [Persson \(1988\)](#) is prior to [Boroson & Green \(1992\)](#) and thereby does not use the same Fe II template as [Marinello et al. \(2016\)](#). Also, the analysis of the spectra for sources observed other than the [Persson \(1988\)](#) use Lorentzian profiles (e.g., [Sulentic et al. 2002](#); [Cracco et al. 2016](#); [Negrete et al. 2018](#)) to fit the $\text{H}\beta$ profile that is typically considered for NLS1s. This additionally introduces a bias in the fluxes and FWHM measured, increasing the values of the ratios compared to the [Persson \(1988\)](#) sample.

3.3. R_{CaT} vs. R_{FeII} : photoionization modelling

The results of our photoionization simulations using CLOUDY facilitates the comparison of the R_{CaT} and R_{FeII} to those compiled in our catalogue as described in Sec. 2.1. We extract the modelled data from the regions as shown in Figure 1 and plot them along with the data from our observed sample. This is shown in Figure 3.

The two panels of Figure 3 show the correlation between the R_{CaT} vs. R_{FeII} both from the observations and from our base model from CLOUDY. The two figures are identical except that the left panel shows the modelled data-points color-coded (and with increasing point-size) as a function of the ionization parameter, while the right panel shows the same data as a function of the cloud density. Points representing the model cover well the central part of the observational plot, although they do not extend far enough to cover either tail of the observed distribution. Higher concentration of the theoretical points partially accounts for the disagreement with the linear slope for the best-fit to the R_{CaT} - R_{FeII} correlation obtained from the observational sample. In the left panel, we see that the maximum R_{FeII} is obtained for ionization parameters, $-2.0 \lesssim \log U \lesssim -1.75$. For the maximum in R_{CaT} , this value is slightly lower, $-2.75 \lesssim \log U \lesssim -2.25$. From the modelled data, there is a clear truncation in the R_{CaT} around $\log R_{\text{CaT}} \approx -0.5$. Similarly, in the right panel, we find that the cloud density required for the maximum R_{FeII} is $n_{\text{H}} \sim 10^{12} \text{ cm}^{-3}$ which reconfirms the conclusions from our previous works (see [Panda et al. 2020](#), are references therein). This value of cloud density is also consistent with maximising the R_{CaT} emission in our base model. These results are consistent with the findings from [Martínez-Aldama et al. \(2015a\)](#) who have suggested that the CaT emitting region is located at the outer part of a high-density BLR. For the quoted values of U and n_{H} , applying the standard photoionization theory, this corresponds to a radial scale⁵, $r \lesssim 0.1 \text{ pc}$. Although, in our base model, increasing the density above this limit ($n_{\text{H}} \gtrsim 10^{12} \text{ cm}^{-3}$) leads to a drop in both R_{FeII} and R_{CaT} emission similar to what was deduced from the ionization case (see also Figure 11). Thus, at least for the strong Fe II emitters, densities higher than 10^{12} lead to contradictory results. We test these hypotheses in the following sections by varying the physical parameters in our CLOUDY models.

Throughout the paper, we utilize only the intensity ratios for the two ionic species and interpret the results based on these estimates. Another important quantity is the equivalent width (EW) of the line which gives a quantitative measure of the spectral feature. In the context of this work, we find that the $\text{I}(\text{Fe II})/\text{I}(\text{H}\beta) \sim$

⁵ The number of ionizing photons for I Zw 1 is derived from the bolometric luminosity, $L_{\text{bol}} \sim 4.32 \times 10^{45} \text{ erg s}^{-1}$, assuming that the net ionizing photon flux, $Q(H) = L_{\text{bol}}/h\nu$, where the $h\nu \sim 1$ Rydberg ([Wandel et al. 1999](#); [Marziani et al. 2015](#)). See also the description of the product of ionization parameter and density for our base model in the appendix of this paper (Sec. A).

$EW(\text{Fe II})/EW(\text{H}\beta)$ (where, I denotes the line intensity). This is same for the CaT. We note that, in the context of photoionization, the EW can be adjusted by changing the covering fraction in the models to match the observed line widths. The problem to reproduce the EW of Low Ionization Lines has been discussed in the literature before. Either additional mechanical heating is necessary (e.g. Collin-Souffrin et al. 1986; Joly 1987), or multiple cloud approach, with part of the radiation scattered/re-emitted between different clouds, or BLR does not see the same continuum as the observer (e.g. Korista et al. 1997). Previous estimates of the BLR size based on the ionization parameter gave much larger values than the reverberation measurements. All this may not affect the line ratios as much as the line EW.

3.3.1. Effect of the metallicity

In Panda et al. (2018), we found that the increase in the metallicity in the BLR cloud leads to an increase in the net Fe II emission. This is shown also in the earlier works from Hamann & Ferland (1992); Leighly (2004) and was later extended in Panda et al. (2019a,b, 2020) to explain the high Fe II-emitters⁶ in the main sequence of quasars. In the base model for the R_{CaT} versus R_{FeII} , the modelled objects are unable to explain the highest emitters ($\log R_{\text{FeII}} \gtrsim 0.2$) as well as the very-low emitters ($\log R_{\text{FeII}} \lesssim -0.6$).

We investigate this effect by testing with two different cases other than the solar abundances, i.e. (a) with sub-solar case (see Punsly et al. 2018 for the analysis of a low Fe II emitter implying slightly sub-solar metallicity) where we assume a net metallicity of $Z = 0.2Z_{\odot}$ (see top-left panel of Figure 4); and (b) with super-solar case where we assume a net metallicity of $Z = 5Z_{\odot}$ (see top-right panel of Figure 4). The super-solar values of metallicities have been studied and confirmed in Negrete et al. (2012); Panda et al. (2019b, and references therein).

For (a) $Z = 0.2Z_{\odot}$ (see top-left panel in Figure 4), we see that the sources that are at the lower end of the observed sample's best-fit correlation can now be explained with the considered range of $\log U - \log n_{\text{H}}$ values, down to $\log R_{\text{FeII}} \sim -0.2$. The model is unable to cover the lower-end ($\log R_{\text{CaT}} \lesssim -1.25$) for R_{CaT} emission, especially the sources from the Persson (1988) sample, and correspondingly for $R_{\text{FeII}} \lesssim -0.6$ (apart from one modelled data-point, i.e. $\log U = -1.5$, with $\log n_{\text{H}} = 13.0$). Defined trends almost tangential to the best-fit line can be seen which highlight the increasing R_{CaT} with de-

creasing ionization parameter. Each of these trends corresponds to a particular value of the cloud density (see also the top-left panel of Figure 6 where the modelled data are shown as a function of the cloud density). The super-solar case and the cases with higher column densities reiterate this trend (see Sec. 3.3.2). For each of the segments, the peak values correspond to a $\log U \cdot n_{\text{H}} = 9.75$ creating an impression of truncation in the maximum R_{CaT} obtained from this model.

In case (b) $Z = 5Z_{\odot}$, none of the observed sources can be modelled with this scaling in the metallicity. The entirety of the modelled data shifts to the higher R_{FeII} (and correspondingly higher R_{CaT}), even though the modelled data points stay on top of the observed sample's best-fit correlation.

This confirms the role of metallicity as a scaling parameter, where an increasing metallicity enhances both CaT and Fe II emission. We showed here the results from two representative cases ($Z = 0.2Z_{\odot}$ and $Z = 5Z_{\odot}$) apart from the base model at solar metallicity. The almost linear scaling of R_{CaT} and R_{FeII} values in terms of the increasing metallicity provides constraints on this parameter based on the observed sample. Thus, a metallicity value $Z_{\odot} < Z < 5Z_{\odot}$ can explain high Fe II emitters in our observed sample. Although, the exact nature of the effect of the metallicity on the trends observed is still not certain. We expect that, on top of the effect of metallicity, sources like the PHL1092 – which is the highest Fe II emitting source in our sample and also accreting at a very high rate ($L_{\text{bol}}/L_{\text{Edd}}=1.24$, Marinello et al. 2020), can be modelled with an appropriate incident continuum, one that has a relatively higher number of energetic photons ($\gtrsim 1$ Ryd). As has been found in recent works (Ferland et al. 2020; Panda et al. 2019a), the role of the soft X-ray excess is important to extract emission, especially from the low ionization lines such as Fe II, and the shape of the ionizing continuum is a crucial ingredient in boosting the net estimate for R_{FeII} and R_{CaT} alike. This will be explored in a future work.

3.3.2. Effect of the cloud column density

After the release of the Persson (1988) sample with both CaT and H β coverage that allowed the measurement of R_{FeII} and R_{CaT} for the same sources, Joly (1989) and Ferland & Persson (1989) performed theoretical analyses using photoionization to understand the relations involving Fe II, H β and CaT. Ferland & Persson (1989) made a series of photoionization calculations, including heating due to free-free and H $^{-}$ absorption. These processes couple the NIR to millimeter continuum with emitting gas and are often the main agents heating the clouds at large column densities. They concluded

⁶ Sources with $R_{\text{FeII}} \gtrsim 1$, which essentially belong to the NLS1s type with $\text{FWHM}(\text{H}\beta) \leq 2000 \text{ km s}^{-1}$ (see Marziani et al. 2020, and references therein).

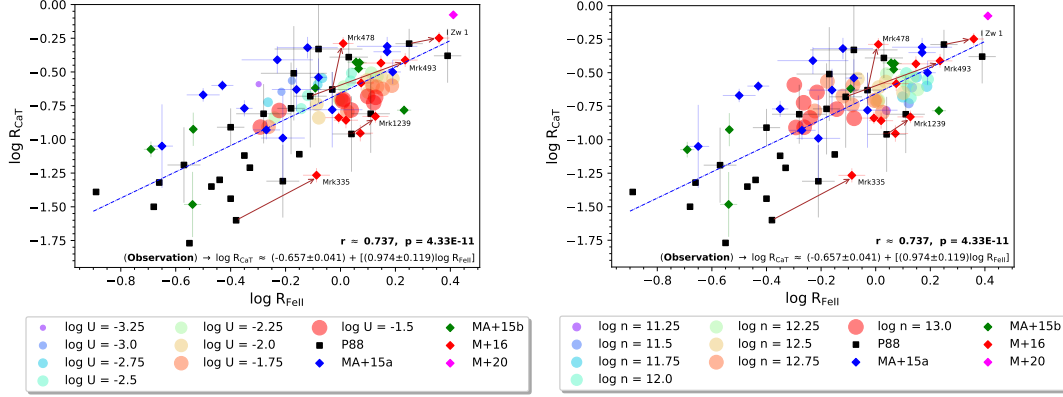


Figure 3. LEFT: Observational measurements (with errors) for R_{FeII} and R_{CaT} are from Persson (1988) (black squares), Martínez-Aldama et al. (2015a) (blue diamonds), Martínez-Aldama et al. (2015b) (green diamonds), Marinello et al. (2016) (red diamonds) and for PHL 1092 estimates from Marinello et al. (2020) (magenta diamond). The best fit for the observational sample is shown with a dashed blue line and also reported on the plot with corresponding Pearson’s correlation coefficients and null probabilities (p-values). The arrows show the shift in the R_{CaT} and R_{FeII} estimates from older (Persson 1988) observations to newer, higher S/N observations (Marinello et al. 2016) for the five common sources with R_{CaT} and R_{FeII} estimates. Data points from the photoionization modelling at solar abundance ($Z=Z_{\odot}$) are shown as a function of ionization parameter (U) in log-scale (i.e. Base Model). The column density (N_{H}) for the model is assumed to be at 10^{24} cm^{-2} . RIGHT: Data points from the photoionization modelling at solar abundance ($Z=Z_{\odot}$) are shown as a function of cloud density (n_{H}) in log-scale. Rest-frame parameters are identical to the left panel.

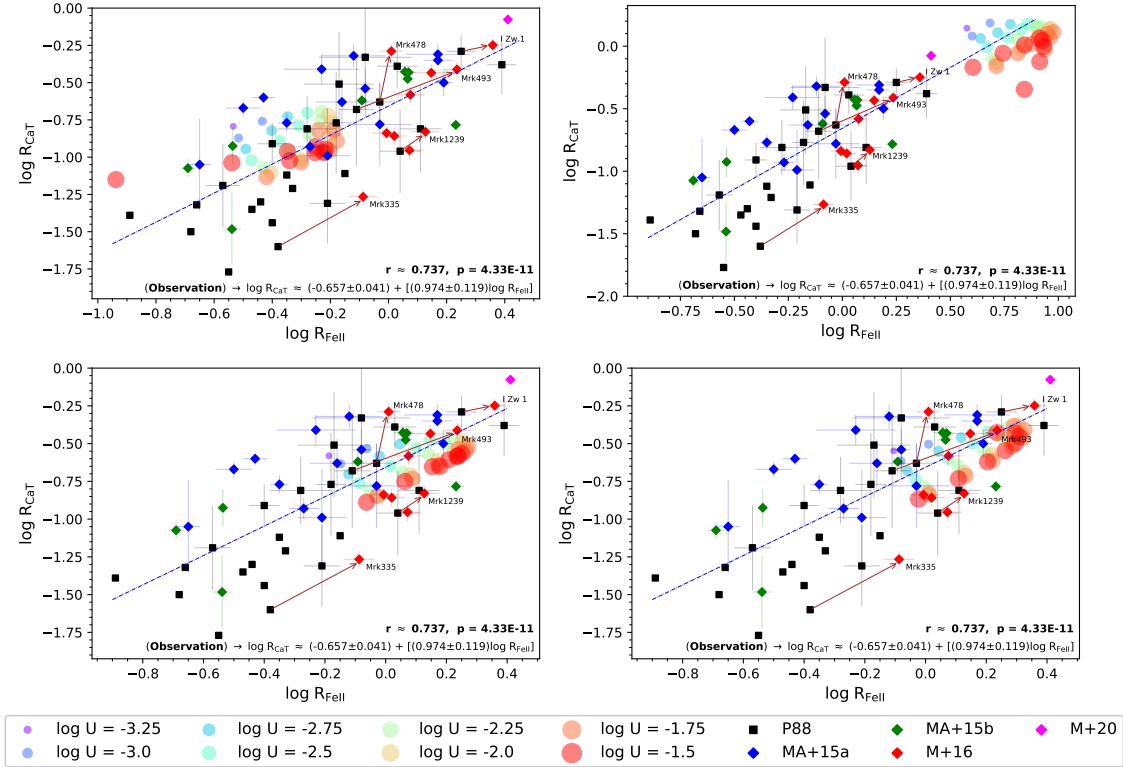


Figure 4. TOP LEFT: Same as left panel of Figure 3 at $Z=0.2Z_{\odot}$. Data points from the CLOUDY model are shown as a function of ionization parameter (U) (in log-scale). TOP RIGHT: Same as previous panel but at $Z=5Z_{\odot}$. BOTTOM LEFT: Same as left panel of Figure 3 but at column density, $N_{\text{H}}=10^{24.5} \text{ cm}^{-2}$. BOTTOM RIGHT: Same as previous panel but at column density, $N_{\text{H}}=10^{25} \text{ cm}^{-2}$.

that no matter the ranges of density and ionization parameters considered, the observed CaT emission cannot be modelled with relatively thin clouds, i.e. with column densities $\sim 10^{23} \text{ cm}^{-2}$. They found that the gas emitting the CaT emission lines is basically the same that is responsible for Fe II emission, although because of the lower ionization potential⁷, $\sim 3.1 \text{ eV}$ (see Figure 1 in Azevedo et al. 2006) as compared to Fe II's $\sim 5.5 \text{ eV}$ (see Figure 13 in Shapovalova et al. 2012) the CaT emission arises from regions that are deeper within the neutral zone. This is also explained in the Figure 7 from Ferland & Persson (1989), where they find that for an assumed column density, $N_H = 10^{24.5} \text{ cm}^{-2}$ and above, the R_{FeII} leads the R_{CaT} by a factor of ~ 1.6 with a much extended emitting region by a factor of $\sim 3\text{-}30$. The authors have also suggested that such large column densities could be related to the presence of wind or corona above the accretion disk.

We adopt this idea by considering two additional cases with increased column densities with respect to our base model: (a) $N_H = 10^{24.5} \text{ cm}^{-2}$ (see lower-left panel of Figure 4), and (b) $N_H = 10^{25} \text{ cm}^{-2}$ (see lower-right panel of Figure 4). Now, with the increase in N_H from 10^{24} to $10^{24.5} \text{ cm}^{-2}$, the bulk of the modelled data shifts to higher values in both R_{FeII} and R_{CaT} (by $\sim 32\%$ in R_{FeII} and $\sim 12\%$ in R_{CaT} , with respect to the base model). Similar to the low-metallicity case ($Z=0.2Z_\odot$), we see defined trends that show increasing R_{CaT} with decreasing ionisation parameter and the peak values in each trend correspond to a $\log U \cdot n_H = 9.75$ (see also the lower panels of Figure 6). The highest values of ionization parameters (i.e., $\log U = -1.5$) form a lower wall parallel to the best-fit relation as a function of varying densities. The data-point for the lowest R_{CaT} recovered ($\log R_{\text{CaT}} \sim -0.889$) for this parallel trend corresponds to the highest density ($\log n_H = 13.0 \text{ cm}^{-3}$), implying that, for a fixed luminosity, the product of the ionization parameter ($\log U = -1.5$) and density ($\log n_H = 13.0 \text{ cm}^{-3}$) corresponds to the smallest BLR radius⁸ ($\sim 0.01 \text{ pc}$). There's an increase in the maximum R_{FeII} recovered in this model ($\log R_{\text{FeII}} \sim 0.272$) which is almost consistent with the R_{FeII} value estimated for I Zw 1 from the older observations (≈ -0.25 , Persson 1988).

For (b) $N_H = 10^{25} \text{ cm}^{-2}$, there's a further shift in the bulk of the modelled data (by $\sim 50\%$ in R_{FeII} and $\sim 27\%$ in R_{CaT} , with respect to the base model). The maximum R_{FeII} recovered ($\log R_{\text{FeII}} \sim 0.326$) increases by

$\sim 56\%$ compared to the base model. For the R_{CaT} , the maximum value ($\log R_{\text{CaT}} \sim -0.374$) went up by a similar factor ($\sim 53\%$) although even with this model, we are unable to account for the R_{FeII} and R_{CaT} measurements for the highest Fe II emitting sources in our sample, i.e., PHL1092 (shown with a magenta diamond), I Zw 1 estimate from Marinello et al. (2016) and Mrk231 from Persson (1988). There is a clear U-turn feature observed in the higher ionization cases ($\log U = -1.5$ and -1.75), where the maximum R_{FeII} values corresponds to a singular cloud density, $\log n_H = 11.75$ and drops when going in either direction in terms of the density. With an additional increase in the column density ($10^{25.5} \lesssim N_H \lesssim 10^{26} \text{ cm}^{-2}$), we can extend the correlation to R_{FeII} values consistent with the ones of PHL1092 and others, but then the optically-thin approximation ($\tau \sim 1$) assumed in this work is no longer applicable.

We conclude that lower column densities of the order of 10^{24} cm^{-2} are sufficient for the low Fe II–Ca II emitters, yet higher column densities ($\gtrsim 10^{24.5} \text{ cm}^{-2}$) are required for the strong Fe II–Ca II emitters ($R_{\text{FeII}} \gtrsim 1$). It is evident from our analysis that fitting the observed trends requires a coupling between the column density and metallicity. Increasing the values for both these parameters allows to recover higher R_{FeII} and R_{CaT} estimates. On the other hand, lowering them recovers the low emitters. We explore this dependence of column density and metallicity in more detail in a subsequent work (Panda 2020).

In Figure 5, we combine all the modelled estimates for R_{FeII} and R_{CaT} for the various cases described until now, i.e., the base model with $Z=Z_\odot$ and $N_H = 10^{24} \text{ cm}^{-2}$, two additional cases of metallicity at $N_H = 10^{24} \text{ cm}^{-2}$: (i) $Z = 0.2 Z_\odot$; and (ii) $Z = 5Z_\odot$, and, two additional cases of column densities at $Z=Z_\odot$: (i) $N_H = 10^{24.5} \text{ cm}^{-2}$; and (ii) $N_H = 10^{25} \text{ cm}^{-2}$. Combining all the modelled estimates together, the best-fit relation⁹ between the R_{FeII} and R_{CaT} is given as:

$$\log \left(\frac{\text{CaT}}{\text{H}\beta} \right) \approx (0.78 \pm 0.022) \log \left(\frac{\text{Fe II}}{\text{H}\beta} \right) - (0.659 \pm 0.009) \quad (5)$$

which has a Pearson's correlation coefficient, and provide a much better agreement with the observed measurements with a tighter correlation ($r \approx 0.935$). $r \approx 0.935$, and a p-value $< 2.2 \times 10^{-16}$. The intrinsic scatter for the slope in the modelled best-fit is quite low, highlighting the robustness of the fit. The best-fit slope brings the correlation closer to the slope of the observed

⁷ the IPs are retrieved from the NIST Atomic database https://physics.nist.gov/PhysRefData/ASD/lines_form.html

⁸ we refer the reader to Panda (2020) for more details on the estimation of the radial sizes in the context of this work.

⁹ The best-fit relation is obtained using the *lm* routine in R reported with standard errors.

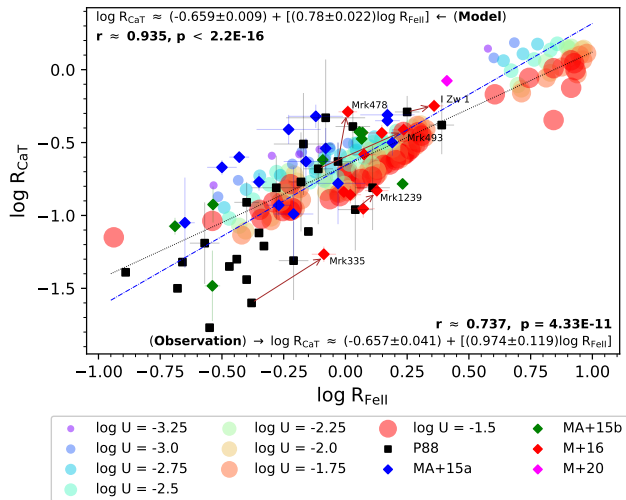


Figure 5. Same as the left panel of Figure 3 with modelled data combined from the previous correlation plots, i.e. Figure 3 (left panel) and all panels from Figure 4. Data points from the CLOUDY models are shown as a function of *ionization parameter* (U in log-scale) identical to the left panel of Figure 3. The best fits for the observational sample (dashed blue) and for the modelled data points (dotted black) and also reported on the plot with corresponding Pearson’s correlation coefficients and null probabilities (p-values).

best-fit correlation (to 1.63σ , where $\sigma=0.119$ is the standard deviation for the observed slope).

Finally, we note that for all the photoionization models, we assumed equal weights per grid point (see Figure 1), and hence, an uniform coverage. This assumption affects the best fit obtained from each individual model that is considered in the paper - this is the reason why we opted not to assign the best-fits to the modelled data in the correlation plots where we show single models (Figures 3, 4, 6 and 11). For these single models, this is a simplistic assumption, one that is influenced by any *un-uniform* concentration of the ionic species within the BLR cloud. For example, in Figure 7, we show how the best-fit slope gets affected when the concentration of one of the grid point has a preferential weightage (here, the grid point in consideration is assigned a weight factor 10, keeping the weights for the remaining points at unity). In this example, we considered three individual points from the R_{FeII} -based panel in our Figure 1 which are also highlighted in the inset plots for each panel of the Figure 7. The effect of this un-uniform weightage can be clearly gauged looking at the change in the slopes for the resulting fits to the modelled data in each case.

On the contrary, when all the models are combined (the base model with $Z=Z_{\odot}$ and $N_H = 10^{24} \text{ cm}^{-2}$, two additional cases of metallicity at $N_H = 10^{24} \text{ cm}^{-2}$: (i) $Z = 0.2 Z_{\odot}$; and (ii) $Z = 5Z_{\odot}$, and, two additional cases of

column densities at $Z=Z_{\odot}$: (i) $N_H = 10^{24.5} \text{ cm}^{-2}$; and (ii) $N_H = 10^{25} \text{ cm}^{-2}$), the effect of these added weights is almost negligible (see modelled best fits in Figure 8), confirming the robustness of the best-fit estimated for the combined models (see Equation 5).

4. DISCUSSIONS

We confirm the strong correlation between the strengths of two emission lines species, the optical Fe II and the NIR CaT, both from observations and photoionization modelling. We establish a new best-fit relation for the correlation between the R_{CaT} and R_{FeII} for an updated catalogue of quasars with measurements for both these species (see Equation 4). With the inclusion of newer observations, we span a wider and more extended parameter space and we test this with our photoionization models using CLOUDY computations parametrized by ionization parameter (U), cloud hydrogen density (n_H), metallicity (Z) and the size of the cloud constrained by the column density (N_H); for a representative ionizing continuum shape taken from the broad-band photometric data for I Zw 1, a prototypical NLS1 source. These results are qualitative and the nature of the effect of these physical parameters needs to be further investigated on a source-by-source basis.

Recent studies have found connection between high accretion rates and high column densities in the absorbing medium (Ricci et al. 2017). NLS1s have been shown to have intrinsically higher accretion rates (Du & Wang 2019, and references therein) and with higher column densities, such as, an additional prospect of the high Fe II emitting NLS1s being Compton thick sources, i.e. $N_H > 10^{24} \text{ cm}^{-2}$ going upto $N_H \sim 10^{26} \text{ cm}^{-2}$ (Sazonov et al. 2015).

These scenarios need to be tested in the future in the context of the present work.

4.1. Effect of a different SED

For generality, we used a representative ionizing continuum shape for I Zw 1. This is a prototypical NLS1 source which has been extensively studied for decades (Oke & Shields 1976; Boroson & Green 1992). Our results confirm the strong correlation between R_{CaT} versus R_{FeII} , yet there are quite a few outliers from the observational viewpoint, such as Mrk335 and PHL1092 among others. It has been pointed that the dependence of the outer radius of the BLR (i.e. the dust sublimation radius) to the bolometric luminosity (Barvainis 1987; Koshida et al. 2014), and, the optical reverberation-mapped BLR radius (equivalent to the inner radius of the BLR) dependence on the monochromatic luminosity (Bentz et al. 2013) is related to the uncertainties on the

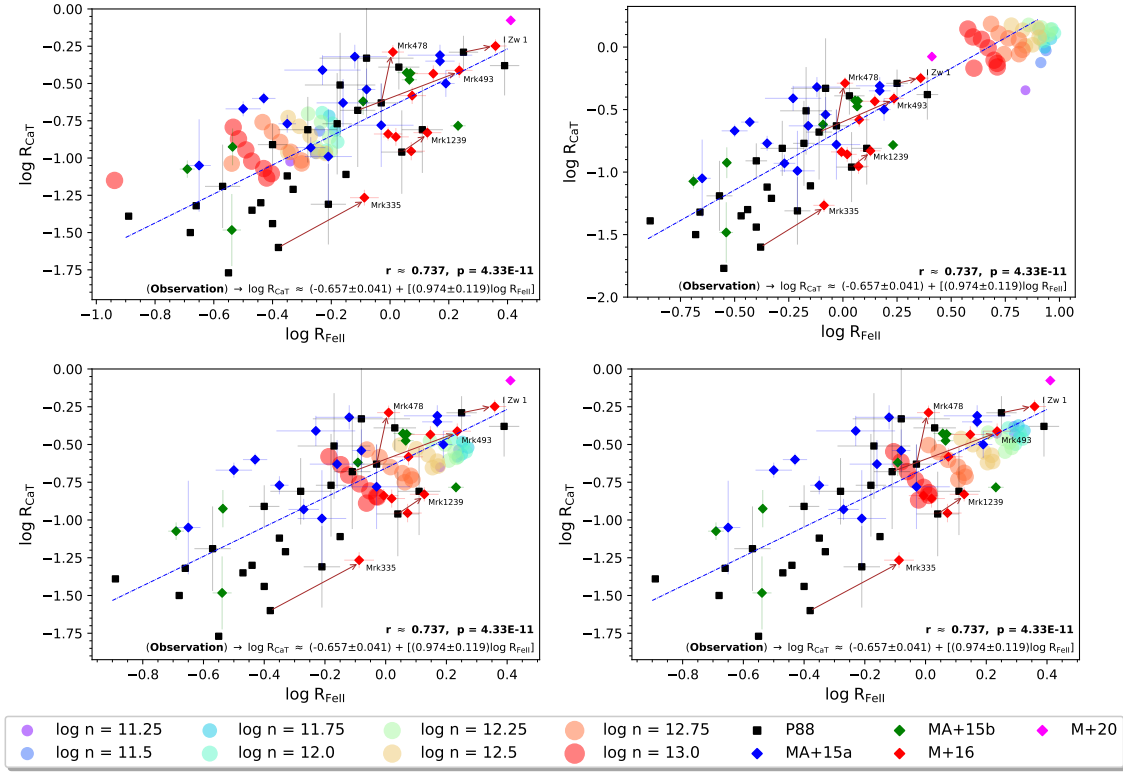


Figure 6. TOP LEFT: Same as top left panel of Figure 4, i.e. at $Z = 0.2Z_{\odot}$ and $N_{\text{H}} = 10^{24} \text{ cm}^{-2}$. TOP RIGHT: Same as previous panel but at $Z = 5Z_{\odot}$. BOTTOM LEFT: Same as bottom left panel of Figure 4, i.e. at $Z = Z_{\odot}$ and $N_{\text{H}} = 10^{24.5} \text{ cm}^{-2}$. BOTTOM RIGHT: Same as previous panel but at $N_{\text{H}} = 10^{25} \text{ cm}^{-2}$. Modelled points from CLOUDY are color-coded here as a function of *cloud density* (n_{H}).

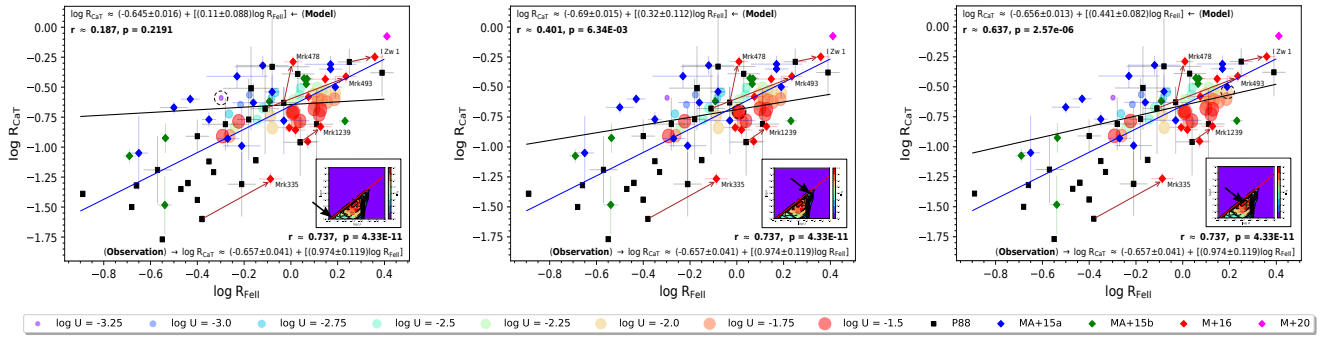


Figure 7. Effect of un-uniform weightage associated with three individual grid points in the base model ($Z=Z_{\odot}$, $N_{\text{H}} = 10^{24} \text{ cm}^{-2}$). Each of the three panels highlight a particular grid point (the location of the grid point is marked in the inset plot and also marked with dashed circle). The grid point in consideration is assigned a weight factor 10, keeping the weights for the remaining points at unity. The best fits for the observational sample (dashed blue) and for the modelled data points (dotted black) and also reported on the plot with corresponding Pearson's correlation coefficients and null probabilities (p -values).

SED of the source (Netzer 2020). We need to account for differences in the SED shapes that has a strong impact on the effective Fe II production (Panda et al. 2019b, 2020) and simultaneously on the CaT emission.

To test this aspect, we considered the SED for this source including the X-ray emission (shown in blue in

Figure 9) procured from NED¹⁰ and compare it against the one used in this paper (obtained from Vizier; shown in red in Figure 9). We have incorporated the two SEDs by interpolating the photometric data as they are provided in the databases. We repeated our analysis using

¹⁰ NASA/IPAC Extragalactic Database.

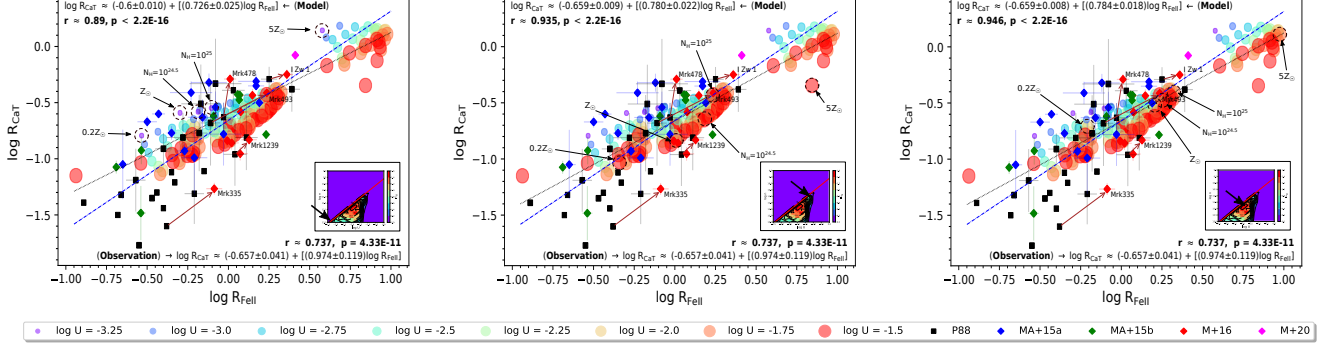


Figure 8. Effect of un-uniform weightage associated with three individual grid points in all five models combined (the base model with $Z=Z_{\odot}$ and $N_H = 10^{24} \text{ cm}^{-2}$, two additional cases of metallicity at $N_H = 10^{24} \text{ cm}^{-2}$: (i) $Z = 0.2 Z_{\odot}$; and (ii) $Z = 5Z_{\odot}$, and, two additional cases of column densities at $Z=Z_{\odot}$: (i) $N_H = 10^{24.5} \text{ cm}^{-2}$; and (ii) $N_H = 10^{25} \text{ cm}^{-2}$). Each of the three panels highlight a particular grid point (same as in Figure 7) for each of the five models (the location of the grid point is marked in the inset plot and also marked with dashed circle). The grid point for each models in consideration are assigned a weight factor 10, keeping the weights for the remaining points at unity. The best fits for the observational sample (dashed blue) and for the combined modelled data points (dotted black) and also reported on the plot with corresponding Pearson's correlation coefficients and null probabilities (p-values).

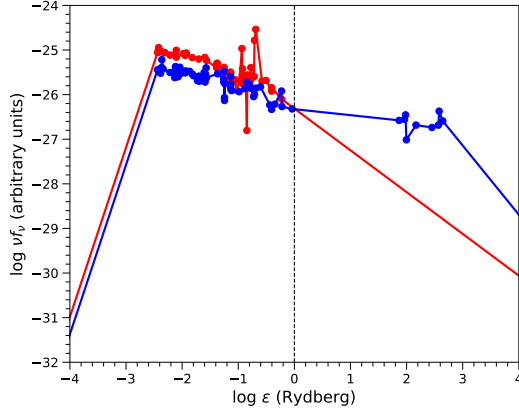


Figure 9. Comparison of the spectral energy distributions (SEDs) for I Zw 1. The distribution shown in red represents the original SED considered and the other one (in blue) where the SED also includes the X-ray data. The emitted power in arbitrary units is plotted as a function of the photon energy in Ryd. The SEDs have been normalised at $\log \epsilon = 0$ which is shown with a black dashed line.

the *blue* SED and recovered similar agreement with the observational sample, although the presence of the more energetic photons in excess of 1 Rydberg compared to the *red* SED lifts the overall R_{FeII} and R_{CaT} estimates (the maximum R_{FeII} recovered in the base model with the *blue* SED rises to 1.8 from 1.6, the latter is obtained from the *red* SED. Similarly for R_{CaT} , the maximum rises to 0.45 from 0.35). Combining all the modelled estimates together, the best-fit relation between the R_{FeII}

and R_{CaT} for the *blue* SED is given as:

$$\log \left(\frac{\text{CaT}}{\text{H}\beta} \right) \approx (0.456 \pm 0.036) \log \left(\frac{\text{Fe II}}{\text{H}\beta} \right) - (0.586 \pm 0.010) \quad (6)$$

which has a Pearson's correlation coefficient, $r \approx 0.612$, and a p-value $< 2.2 \times 10^{-16}$. The intrinsic scatter for the modelled best-fit again remains quite low as compared to the observed data although the slope here is much shallower than what was obtained from the models that used the *red* SED (see Figure 12). This highlights the importance of the shape of the incident continuum in the study of the BLR, especially for the low-ionization lines' emission. The standard photoionization theory is based on the assumption that the BLR and the distant observer see the same ionizing continuum. This assumption has been questioned in many recent works (Wang et al. 2014; Gaskell et al. 2019; Ferland et al. 2020, and references therein) highlighting the issue of anisotropic radiation from the accretion disk. This necessitates further investigation.

4.2. Effect of different dust prescriptions

Keeping rooted to Nenkova et al. (2008) formalism, for a different dust composition, e.g. more carbon grains and/or larger grain sizes, the characteristic T_{sub} could be $\sim 2000 \text{ K}$. This gives us a dust sublimation radius: $R_d = 0.189 \sqrt{L/10^{45}} \text{ pc}$. If we apply this to obtain the parameter space similar to Figure 1, we will essentially shrink the non-dusty region by a factor ~ 2.12 . This will drop the emission corresponding not only for the lower ionization parameters but also for the low-density models with higher ionisation parameters. In principle, the dusty region consists of dust grains with a distribution of

the said properties (sublimation temperature and grain size) which makes the modelling even more complicated. Added to this, is the confirmation of clumpiness in the dusty regions (Hönig & Kishimoto 2010) which contests the relevance of the Nenkova et al. (2008); Barvainis (1987) relations which assume a smooth distribution of dust in the torus. This needs to be tested in the context of our analyses.

We incorporated the Nenkova et al. (2008) prescription to compute the sublimation radius which inherently assumes a simplified dust grain size, $a = 0.05 \mu\text{m}$, and, a slight modification in the exponent for the dust temperature, -2.6 instead of -2.8 (the latter is from the original Barvainis (1987) assuming a Planckian distribution for the dust grains). Under the assumption of $a = 0.05 \mu\text{m}$, the ratio of the sublimation radius obtained from both descriptions is only a function of the dust temperature,

$$\frac{R_{sub,N}}{R_{sub,B}} = 0.973 \times \left(\frac{T_{sub}}{1500K} \right)^{0.2} \quad (7)$$

where, the subscripts N = Nenkova et al. (2008) and B = Barvainis (1987) prescriptions. The radius obtained from both formalisms becomes equal for a dust temperature around 1780 K, and, only grows by 3% for a dust temperature around 2000 K.

An increase in the dust grain size can also lead to the shrinking of the dust sublimation radius. Baskin & Laor (2018b) have shown that with a high enough particle density ($\sim 10^{10} \text{ cm}^{-3}$), larger grains of the order of $1 \mu\text{m}$ can result in a sublimation radius shrunk to the radius of the broad-line region. Such an effect will curtail the emission from the far-side of the BLR cloud. High luminosity plays a vital role here to counter this effect. Contrary to our simplistic approach to determine a singular dust sublimation radius, past works (Baskin & Laor 2018b, and references therein) have pointed towards the dependence of the dust temperature on the gas density, grain size and the chemical composition which implies selective dust grain evaporation. This suggests a dust *sublimation zone* instead of a unique value for the R_{sub} . Additionally, for the dust prescription, we have assumed the source luminosity as per I Zw 1, i.e. $L_{bol} \sim 4.32 \times 10^{45} \text{ erg s}^{-1}$. For our observational sample, we have the range of monochromatic luminosity such that, $42.5 < \log L_{5100} < 46.8$, with a mean value at 44.65 which is not far from I Zw 1's luminosity ($\log L_{5100} = 44.54$). Thus, scaling the L_{5100} for the whole sample using the bolometric correction factor, we get $44.0 < \log L_{bol} < 47.44$. Substituting this range in Equation 3 (assuming $T_{sub}=1500 \text{ K}$), the range of sublimation radii (in parsecs) is $0.127 \leq R_{sub} \leq 6.654$. The lower limit shrinks the non-dusty BLR by a factor

of ~ 6.5 (with respect to the $R_{sub} = 0.83 \text{ pc}$, obtained for I Zw 1). This can further curb the overall emission derived from Fe II and CaT considering only the dustless region of the BLR. On the other hand, at the high luminosity end the sublimation radius gets pushed further (by ~ 8 times), allowing more Fe II and CaT ions to compete for the incoming photons emanated by the accretion disk and hence, increasing the emission from these species. For example, in the case of PHL1092, with $L_{5100} \sim 7.638 \times 10^{44} \text{ erg s}^{-1}$ (Marinello et al. 2020) gives a $R_{sub} = 1.138 \text{ pc}$. This is already a 40% increase in the size of the dustless BLR as compared to what has been assumed in this paper. With the inclusion of a proper SED shape mimicking the PHL1092's emission and this increased size for the dustless BLR, the effective R_{FeII} and R_{CaT} values may be achievable. We leave this for a future work.

5. CONCLUSIONS

In this article, we confirm the strong correlation between the strengths of two emission lines species, the optical Fe II and the NIR CaT, both from observations and photoionization modelling. With the inclusion of newer observations, we span a wider and extended parameter space and we test this with our photoionization models using CLOUDY. We summarize the important conclusions derived from this work as following:

- We compile an up-to-date catalogue of 58 sources (including 5 common) with corresponding R_{CaT} and R_{FeII} measurements. We then derive the best-fit correlation for R_{CaT} versus R_{FeII} for our sample (see Equation 4). With the inclusion of newer data, the best-fit correlation is now consistent with simple proportionality between the two quantities. The best fit slope reported by Martínez-Aldama et al. (2015a) was considerably higher (1.33 vs. 1.008 in this paper) but the two values are still consistent within 3σ error.
- We overlay the modelled data from our photoionization models onto the observed measurements and take this a step further by analysing the optimum parametrization that leads to the maximum emissivity for both these species in terms of (a) ionization parameter; and (b) local cloud density. We find that with our base modelling assumptions, i.e. $Z = Z_{\odot}$ and column density $N_H = 10^{24} \text{ cm}^{-2}$, we can quite convincingly explain the mean population amidst the correlation and quantify the range of emission strengths for these two species with this approach.

- We further extend our models by testing the effect of metallicity as a way to explain the range of R_{CaT} and R_{FeII} measurements. We find that the low-Fe II low-CaT emission is well explained by assuming a sub-solar metallicity, such as $0.2Z_{\odot}$ keeping the remaining parameters identical to the base model. On the other hand, for the high-end of the correlation, we tested with a super-solar metallicity ($Z=5Z_{\odot}$) as shown by previous studies (Panda et al. 2020, and references therein). We find that the maximum R_{FeII} values (e.g. I Zw 1 and PHL1092) can be well explained with fairly low metallicities, i.e. $Z \lesssim 5Z_{\odot}$, although above solar values.
- Motivated from past studies (Ferland & Persson 1989), we also involve the effect of increasing the column density and subsequently find increased R_{CaT} and R_{FeII} by a factor of $\sim 20\%$ by enhancing N_H from 10^{24} cm^{-2} to $10^{24.5} \text{ cm}^{-2}$. A further increase of $\sim 20\%$ is seen by assuming an $N_H = 10^{25} \text{ cm}^{-2}$ which gives comparable R_{CaT} and R_{FeII} estimates for the strong-emitting NLS1s. We confirm that an increase in column density relates well with the increased emission for both these species. We clearly find a coupling between the metallicity and column density which leads to increased emission for both CaT and Fe II and bringing the best-fit correlation within 2σ of the observed best-fit relation.
- Finally, we combine all the modelled estimates for R_{FeII} and R_{CaT} for the five cases - the base model with $Z=Z_{\odot}$ and $N_H = 10^{24} \text{ cm}^{-2}$, two additional cases of metallicity at $N_H = 10^{24} \text{ cm}^{-2}$: (i) $Z =$

$0.2 Z_{\odot}$; and (ii) $Z = 5Z_{\odot}$, and, two additional cases of column densities at $Z=Z_{\odot}$: (i) $N_H = 10^{24.5} \text{ cm}^{-2}$; and (ii) $N_H = 10^{25} \text{ cm}^{-2}$, and estimate the joint best-fit (see Equation 5) with a high significance (Pearson's correlation coefficient, $r \approx 0.935$; and a p-value $< 2.2 \times 10^{-16}$). This is in good agreement with the relation given by the observations (see Equation 4).

An increased availability of optical and NIR spectroscopic measurements, especially with the advent of the upcoming ground-based 10-metre-class (e.g. Maunakea Spectroscopic Explorer, Marshall et al. 2019) and 40 metre-class (e.g. The European Extremely Large Telescope, Evans et al. 2015) telescopes; and space-based missions such as the James Webb Space Telescope and the Nancy Grace Roman Space Telescope would further help to accentuate the strong correlation shown by these two ionic species.

ACKNOWLEDGEMENTS

We are grateful to the anonymous referee for his comments and suggestions that helped shape the current version of the manuscript. The project was partially supported by the Polish Funding Agency National Science Centre, project 2017/26/A/ST9/00756 (MAESTRO 9) and MNiSW grant DIR/WK/2018/12. SP would like to acknowledge the computational facility at CAMK and Dr. Paweł Ciecieląg for assistance with the computational cluster. DD acknowledges support from grant PAPIIT UNAM, 113719. We specially thank Alenka Negrete for providing us with the data used in Figure 2 in this paper.

Software: CLOUDY v17.01 (Ferland et al. 2017); MATPLOTLIB (Hunter 2007); NUMPY (Oliphant 2015); R (R Core Team 2019)

REFERENCES

- Azevedo, R., Calvet, N., Hartmann, L., et al. 2006, *A&A*, 456, 225, doi: [10.1051/0004-6361:20054315](https://doi.org/10.1051/0004-6361:20054315)
- Baldwin, J., Ferland, G., Korista, K., & Verner, D. 1995, *ApJL*, 455, L119, doi: [10.1086/309827](https://doi.org/10.1086/309827)
- Barth, A. J., Pancoast, A., Bennert, V. N., et al. 2013, *ApJ*, 769, 128, doi: [10.1088/0004-637X/769/2/128](https://doi.org/10.1088/0004-637X/769/2/128)
- Barvainis, R. 1987, *ApJ*, 320, 537, doi: [10.1086/165571](https://doi.org/10.1086/165571)
- Baskin, A., & Laor, A. 2018a, *MNRAS*, 474, 1970, doi: [10.1093/mnras/stx2850](https://doi.org/10.1093/mnras/stx2850)
- . 2018b, *MNRAS*, 474, 1970, doi: [10.1093/mnras/stx2850](https://doi.org/10.1093/mnras/stx2850)
- Bentz, M. C., Denney, K. D., Grier, C. J., et al. 2013, *ApJ*, 767, 149, doi: [10.1088/0004-637X/767/2/149](https://doi.org/10.1088/0004-637X/767/2/149)
- Boroson, T. A., & Green, R. F. 1992, *ApJS*, 80, 109, doi: [10.1086/191661](https://doi.org/10.1086/191661)
- Bruhweiler, F., & Verner, E. 2008, *ApJ*, 675, 83, doi: [10.1086/525557](https://doi.org/10.1086/525557)
- Collin-Souffrin, S., Dumnont, S., Joly, M., & Pequignot, D. 1986, *A&A*, 166, 27
- Cracco, V., Ciroi, S., Berton, M., et al. 2016, *MNRAS*, 462, 1256, doi: [10.1093/mnras/stw1689](https://doi.org/10.1093/mnras/stw1689)
- Du, P., & Wang, J.-M. 2019, *ApJ*, 886, 42, doi: [10.3847/1538-4357/ab4908](https://doi.org/10.3847/1538-4357/ab4908)

- Dultzin-Hacyan, D., Taniguchi, Y., & Uranga, L. 1999, *Astronomical Society of the Pacific Conference Series*, Vol. 175, Where is the Ca II Triplet Emitting Region in AGN?, ed. C. M. Gaskell, W. N. Brandt, M. Dietrich, D. Dultzin-Hacyan, & M. Eracleous, 303
- Evans, C., Puech, M., Afonso, J., et al. 2015, arXiv e-prints, arXiv:1501.04726. <https://arxiv.org/abs/1501.04726>
- Ferland, G. J., Done, C., Jin, C., Landt, H., & Ward, M. J. 2020, *MNRAS*, 494, 5917, doi: [10.1093/mnras/staa1207](https://doi.org/10.1093/mnras/staa1207)
- Ferland, G. J., & Persson, S. E. 1989, *ApJ*, 347, 656, doi: [10.1086/168156](https://doi.org/10.1086/168156)
- Ferland, G. J., Chatzikos, M., Guzmán, F., et al. 2017, *RMxAA*, 53, 385. <https://arxiv.org/abs/1705.10877>
- Garcia-Rissmann, A., Rodríguez-Ardila, A., Sigut, T. A. A., & Pradhan, A. K. 2012, *ApJ*, 751, 7, doi: [10.1088/0004-637X/751/1/7](https://doi.org/10.1088/0004-637X/751/1/7)
- Gaskell, C. M., Bartel, K., Deffner, J. N., & Xia, I. 2019, arXiv e-prints, arXiv:1909.06275. <https://arxiv.org/abs/1909.06275>
- Goad, M. R., & Korista, K. T. 2015, *MNRAS*, 453, 3662, doi: [10.1093/mnras/stv1861](https://doi.org/10.1093/mnras/stv1861)
- Grevesse, N., Asplund, M., Sauval, A. J., & Scott, P. 2010, *Ap&SS*, 328, 179, doi: [10.1007/s10509-010-0288-z](https://doi.org/10.1007/s10509-010-0288-z)
- Hamann, F., & Ferland, G. 1992, *ApJL*, 391, L53, doi: [10.1086/186397](https://doi.org/10.1086/186397)
- Hönig, S. F., & Kishimoto, M. 2010, *A&A*, 523, A27, doi: [10.1051/0004-6361/200912676](https://doi.org/10.1051/0004-6361/200912676)
- Hu, C., Du, P., Lu, K.-X., et al. 2015, *ApJ*, 804, 138, doi: [10.1088/0004-637X/804/2/138](https://doi.org/10.1088/0004-637X/804/2/138)
- Hunter, J. D. 2007, *Computing in Science and Engineering*, 9, 90, doi: [10.1109/MCSE.2007.55](https://doi.org/10.1109/MCSE.2007.55)
- Joly, M. 1987, *A&A*, 184, 33
- . 1989, *A&A*, 208, 47
- . 1991, *A&A*, 242, 49
- Kishimoto, M., Hönig, S. F., Beckert, T., & Weigelt, G. 2007, *A&A*, 476, 713, doi: [10.1051/0004-6361:20077911](https://doi.org/10.1051/0004-6361:20077911)
- Korista, K., Baldwin, J., Ferland, G., & Verner, D. 1997, *ApJS*, 108, 401, doi: [10.1086/312966](https://doi.org/10.1086/312966)
- Koshida, S., Minezaki, T., Yoshii, Y., et al. 2014, *ApJ*, 788, 159, doi: [10.1088/0004-637X/788/2/159](https://doi.org/10.1088/0004-637X/788/2/159)
- Kovačević, J., Popović, L. Č., & Dimitrijević, M. S. 2010, *ApJS*, 189, 15, doi: [10.1088/0067-0049/189/1/15](https://doi.org/10.1088/0067-0049/189/1/15)
- Leighly, K. M. 2004, *ApJ*, 611, 125, doi: [10.1086/422089](https://doi.org/10.1086/422089)
- Magorrian, J., Tremaine, S., Richstone, D., et al. 1998, *AJ*, 115, 2285, doi: [10.1086/300353](https://doi.org/10.1086/300353)
- Marinello, M., Rodríguez-Ardila, A., Garcia-Rissmann, A., Sigut, T. A. A., & Pradhan, A. K. 2016, *ApJ*, 820, 116, doi: [10.3847/0004-637X/820/2/116](https://doi.org/10.3847/0004-637X/820/2/116)
- Marinello, M., Rodríguez-Ardila, A., Marziani, P., Sigut, A., & Pradhan, A. 2020, *MNRAS*, 494, 4187, doi: [10.1093/mnras/staa934](https://doi.org/10.1093/mnras/staa934)
- Marshall, J., Bolton, A., Bullock, J., et al. 2019, in *Bulletin of the American Astronomical Society*, Vol. 51, 126. <https://arxiv.org/abs/1907.07192>
- Martínez-Aldama, M. L., Dultzin, D., Marziani, P., et al. 2015a, *ApJS*, 217, 3, doi: [10.1088/0067-0049/217/1/3](https://doi.org/10.1088/0067-0049/217/1/3)
- Martínez-Aldama, M. L., Marziani, P., Dultzin, D., et al. 2015b, *Journal of Astrophysics and Astronomy*, 36, 457, doi: [10.1007/s12036-015-9354-9](https://doi.org/10.1007/s12036-015-9354-9)
- Marziani, P., Sulentic, J. W., Negrete, C. A., et al. 2015, *ApSS*, 356, 339, doi: [10.1007/s10509-014-2136-z](https://doi.org/10.1007/s10509-014-2136-z)
- Marziani, P., Sulentic, J. W., Zwitter, T., Dultzin-Hacyan, D., & Calvani, M. 2001, *ApJ*, 558, 553, doi: [10.1086/322286](https://doi.org/10.1086/322286)
- Marziani, P., Dultzin, D., Sulentic, J. W., et al. 2018a, *Frontiers in Astronomy and Space Sciences*, 5, 6, doi: [10.3389/fspas.2018.00006](https://doi.org/10.3389/fspas.2018.00006)
- . 2018b, *Frontiers in Astronomy and Space Sciences*, 5, 6, doi: [10.3389/fspas.2018.00006](https://doi.org/10.3389/fspas.2018.00006)
- Marziani, P., Bon, E., Bon, N., et al. 2019, *Atoms*, 7, 18, doi: [10.3390/atoms7010018](https://doi.org/10.3390/atoms7010018)
- Marziani, P., Dultzin, D., Del Olmo, A., et al. 2020, arXiv e-prints, arXiv:2002.07219. <https://arxiv.org/abs/2002.07219>
- Matsuoka, Y., Kawara, K., & Oyabu, S. 2008, *ApJ*, 673, 62, doi: [10.1086/524193](https://doi.org/10.1086/524193)
- Matsuoka, Y., Oyabu, S., Tsuzuki, Y., & Kawara, K. 2007, *ApJ*, 663, 781, doi: [10.1086/518399](https://doi.org/10.1086/518399)
- Matsuoka, Y., Oyabu, S., Tsuzuki, Y., Kawara, K., & Yoshii, Y. 2005, *PASJ*, 57, 563, doi: [10.1093/pasj/57.4.563](https://doi.org/10.1093/pasj/57.4.563)
- Merloni, A., Bongiorno, A., Bolzonella, M., et al. 2010, *ApJ*, 708, 137, doi: [10.1088/0004-637X/708/1/137](https://doi.org/10.1088/0004-637X/708/1/137)
- Negrete, A., Dultzin, D., Marziani, P., & Sulentic, J. 2012, *ApJ*, 757, 62. <https://arxiv.org/abs/1107.3188>
- Negrete, C. A., Dultzin, D., Marziani, P., & Sulentic, J. W. 2013, *ApJ*, 771, 31, doi: [10.1088/0004-637X/771/1/31](https://doi.org/10.1088/0004-637X/771/1/31)
- . 2014, *Advances in Space Research*, 54, 1355, doi: [10.1016/j.asr.2013.11.037](https://doi.org/10.1016/j.asr.2013.11.037)
- Negrete, C. A., Dultzin, D., Marziani, P., et al. 2018, *A&A*, 620, A118, doi: [10.1051/0004-6361/201833285](https://doi.org/10.1051/0004-6361/201833285)
- Nenkova, M., Sirocky, M. M., Ivezić, Ž., & Elitzur, M. 2008, *ApJ*, 685, 147, doi: [10.1086/590482](https://doi.org/10.1086/590482)
- Netzer, H. 2019, *MNRAS*, 488, 5185, doi: [10.1093/mnras/stz2016](https://doi.org/10.1093/mnras/stz2016)
- . 2020, *MNRAS*, doi: [10.1093/mnras/staa767](https://doi.org/10.1093/mnras/staa767)
- Netzer, H., & Laor, A. 1993, *ApJL*, 404, L51, doi: [10.1086/186741](https://doi.org/10.1086/186741)

- Oke, J. B., & Shields, G. A. 1976, *ApJ*, 207, 713, doi: [10.1086/154540](https://doi.org/10.1086/154540)
- Oliphant, T. 2015, *NumPy: A guide to NumPy*, 2nd edn., USA: CreateSpace Independent Publishing Platform. <http://www.numpy.org/>
- Panda, S. 2020, arXiv e-prints, arXiv:2004.13113. <https://arxiv.org/abs/2004.13113>
- Panda, S., Czerny, B., Adhikari, T. P., et al. 2018, *ApJ*, 866, 115, doi: [10.3847/1538-4357/aae209](https://doi.org/10.3847/1538-4357/aae209)
- Panda, S., Czerny, B., Done, C., & Kubota, A. 2019a, *ApJ*, 875, 133, doi: [10.3847/1538-4357/ab11cb](https://doi.org/10.3847/1538-4357/ab11cb)
- Panda, S., Czerny, B., & Wildy, C. 2017, *Frontiers in Astronomy and Space Sciences*, 4, 33, doi: [10.3389/fspas.2017.00033](https://doi.org/10.3389/fspas.2017.00033)
- Panda, S., Marziani, P., & Czerny, B. 2019b, *ApJ*, 882, 79, doi: [10.3847/1538-4357/ab3292](https://doi.org/10.3847/1538-4357/ab3292)
- . 2020, *Contributions of the Astronomical Observatory Skalnaté Pleso*, 50, 293, doi: [10.31577/caosp.2020.50.1.293](https://doi.org/10.31577/caosp.2020.50.1.293)
- Persson, S. E. 1988, *ApJ*, 330, 751, doi: [10.1086/166509](https://doi.org/10.1086/166509)
- Punsly, B., Marziani, P., Bennert, V. N., Nagai, H., & Gurwell, M. A. 2018, *ApJ*, 869, 143, doi: [10.3847/1538-4357/aaec75](https://doi.org/10.3847/1538-4357/aaec75)
- R Core Team. 2019, *R: A Language and Environment for Statistical Computing*, R Foundation for Statistical Computing, Vienna, Austria. <https://www.R-project.org/>
- Rayner, J. T., Toomey, D. W., Onaka, P. M., et al. 2003, *PASP*, 115, 362, doi: [10.1086/367745](https://doi.org/10.1086/367745)
- Ricci, C., Trakhtenbrot, B., Koss, M. J., et al. 2017, *Nature*, 549, 488, doi: [10.1038/nature23906](https://doi.org/10.1038/nature23906)
- Riffel, R., Rodríguez-Ardila, A., & Pastoriza, M. G. 2006, *A&A*, 457, 61, doi: [10.1051/0004-6361/20065291](https://doi.org/10.1051/0004-6361/20065291)
- Riffel, R. A., Colina, L., Storchi-Bergmann, T., et al. 2016, *MNRAS*, 461, 4192, doi: [10.1093/mnras/stw1609](https://doi.org/10.1093/mnras/stw1609)
- Rodríguez-Ardila, A., Viegas, S. M., Pastoriza, M. G., & Prato, L. 2002, *ApJ*, 565, 140, doi: [10.1086/324598](https://doi.org/10.1086/324598)
- Sazonov, S., Churazov, E., & Krivonos, R. 2015, *Monthly Notices of the Royal Astronomical Society*, 454, 1202, doi: [10.1093/mnras/stv2069](https://doi.org/10.1093/mnras/stv2069)
- Shapovalova, A. I., Popović, L. Č., Burenkov, A. N., et al. 2012, *ApJS*, 202, 10, doi: [10.1088/0067-0049/202/1/10](https://doi.org/10.1088/0067-0049/202/1/10)
- Shen, Y., & Ho, L. C. 2014, *Nature*, 513, 210, doi: [10.1038/nature13712](https://doi.org/10.1038/nature13712)
- Shen, Y., Richards, G. T., Strauss, M. A., et al. 2011, *ApJS*, 194, 45, doi: [10.1088/0067-0049/194/2/45](https://doi.org/10.1088/0067-0049/194/2/45)
- Sigut, T. A. A., & Pradhan, A. K. 2003, *ApJS*, 145, 15, doi: [10.1086/345498](https://doi.org/10.1086/345498)
- Sulentic, J. W., Calvani, M., & Marziani, P. 2001, *The Messenger*, 104, 25
- Sulentic, J. W., Marziani, P., & Dultzin-Hacyan, D. 2000a, *ARA&A*, 38, 521, doi: [10.1146/annurev.astro.38.1.521](https://doi.org/10.1146/annurev.astro.38.1.521)
- Sulentic, J. W., Marziani, P., Zamanov, R., et al. 2002, *ApJL*, 566, L71, doi: [10.1086/339594](https://doi.org/10.1086/339594)
- Sulentic, J. W., Zwitter, T., Marziani, P., & Dultzin-Hacyan, D. 2000b, *ApJL*, 536, L5, doi: [10.1086/312717](https://doi.org/10.1086/312717)
- Sulentic, J. W., del Olmo, A., Marziani, P., et al. 2017, *A&A*, 608, A122, doi: [10.1051/0004-6361/201630309](https://doi.org/10.1051/0004-6361/201630309)
- Verner, E. M., Verner, D. A., Korista, K. T., et al. 1999, *ApJS*, 120, 101, doi: [10.1086/313171](https://doi.org/10.1086/313171)
- Véron-Cetty, M. P., Joly, M., & Véron, P. 2004, *A&A*, 417, 515, doi: [10.1051/0004-6361:20035714](https://doi.org/10.1051/0004-6361:20035714)
- Vestergaard, M., & Wilkes, B. J. 2001, *ApJS*, 134, 1, doi: [10.1086/320357](https://doi.org/10.1086/320357)
- Wandel, A., Peterson, B. M., & Malkan, M. A. 1999, *ApJ*, 526, 579, doi: [10.1086/308017](https://doi.org/10.1086/308017)
- Wang, J.-M., Qiu, J., Du, P., & Ho, L. C. 2014, *ApJ*, 797, 65, doi: [10.1088/0004-637X/797/1/65](https://doi.org/10.1088/0004-637X/797/1/65)

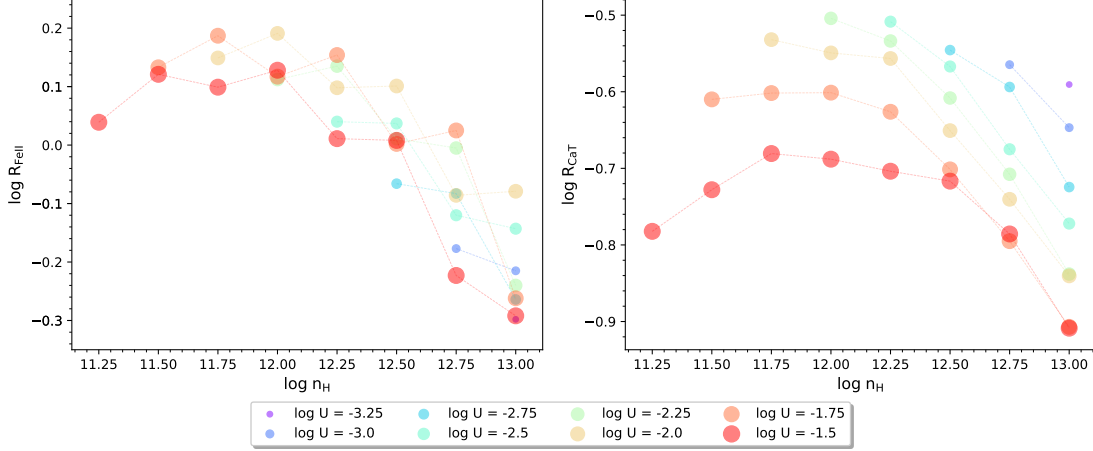


Figure 10. Distribution of densities and ionisation parameters for (a) R_{FeII} , and (b) R_{CaT} . The estimates are for the Base Model as shown in Figure 3.

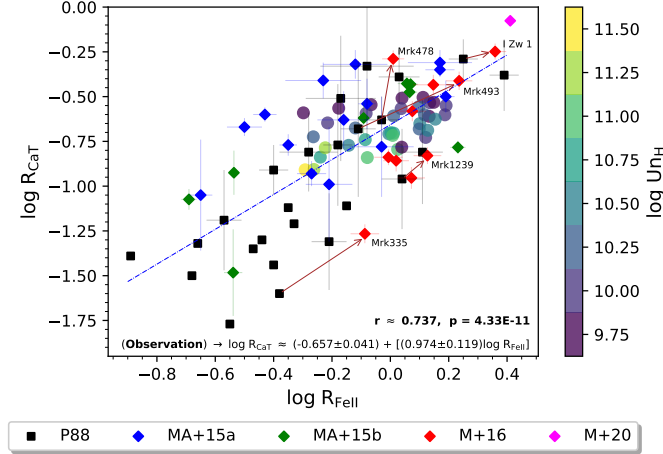


Figure 11. Data points from the photoionization modelling are shown as a function of $U \cdot n_{\text{H}}$ in log-scale. Rest parameters are identical to the left panel of Figure 3.

APPENDIX

A. PRODUCT OF THE CLOUD DENSITY AND IONIZATION PARAMETER

In the panels of Figure 3, we explored the dependence of the effect of the ionization parameter and local cloud density, respectively. The initial idea was to find a way to constrain the sources with respect to these two fundamental physical parameters. However, the dependence on the parameters is clearly non-monotonic which is reflected in the considerable diversity in the distribution when one considers them separately.

Here, we investigate the coupled distribution between the two parameters. As has been previously explored in Negrete et al. (2012, 2014); Marziani et al. (2019), we take the product of the ionization parameter and the local cloud density ($U \cdot n_{\text{H}}$), i.e. the ionizing photon flux, which can be used as an estimator for the size of the BLR (R_{BLR} ; see, e.g. Negrete et al. 2013; Panda 2020 and references therein). In Figure 11, we illustrate this with the modelled data from our base model as shown previously (see both panels of Figure 3) in order to judge if there is a clear trend with respect to $U \cdot n_{\text{H}}$. Rather interestingly, the highest values for the product of U and n_{H} ($\gtrsim 11.25$ in log-scale) correspond to the lowest values of the R_{FeII} ($\log R_{\text{FeII}} \lesssim -0.2$). The values for the corresponding R_{CaT} are among the lowest as well for these conditions ($\log R_{\text{CaT}} \lesssim -0.75$). The highest values for the R_{FeII} ($\log R_{\text{FeII}} \sim 0.2$) are actually obtained for much

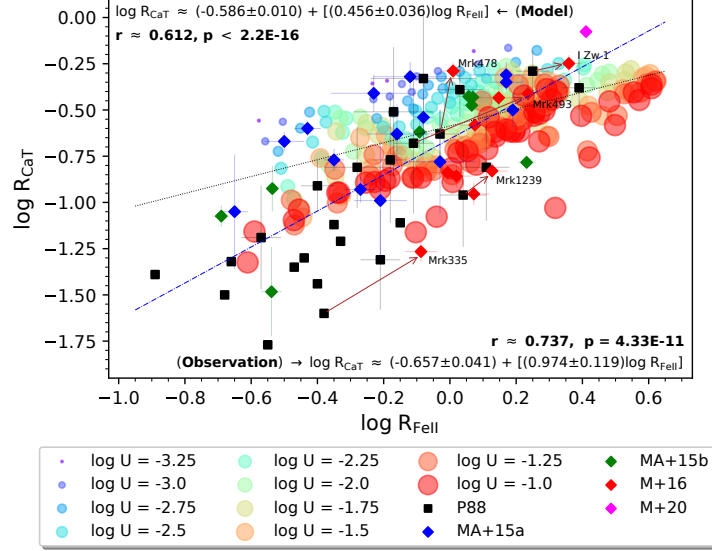


Figure 12. Same as Figure 5 but the models are generated using the incident SED including the X-ray emission (see the blue continuum in Figure 9).

smaller values of the product ($9.75 \lesssim \log U n_{\text{H}} \lesssim 10.25$). This is consistent also for the highest values for the R_{CaT} ($\log R_{\text{CaT}} \lesssim -0.5$) although at slightly lower $U \cdot n_{\text{H}}$, suggesting larger values for the R_{BLR} are required to efficiently produce these ionic species. This implies that, from a strictly photoionizing point of view, the two emitting regions are quite closely related in terms of their distance from the central ionizing source, with the CaT emitting region further out than the Fe II region. Panda et al. (2018, 2019a,b) found that the typical BLR densities to maximise the Fe II emission strength is achieved with higher densities, typically of the order of 10^{12} cm^{-3} . This, for the maximum R_{FeII} value, corresponds to an ionization parameter, $\log U \sim -2.0 \pm 0.25$ while $U \sim -2.25$ maximizes the CaT emission. This is exactly what we see directly from Figure 1. There’s a clear decrease in the $\log U \cdot n_{\text{H}}$ along the best-fit relation, i.e., both the R_{FeII} and R_{CaT} increase with decreasing $\log U \cdot n_{\text{H}}$.

Alternatively, we can look at the dependence on $\log U - \log n_{\text{H}}$ on maximising the R_{FeII} and R_{CaT} as shown in the two panels of Figure 10 which illustrates the variation in the R_{FeII} (left panel) and for R_{CaT} (right panel). The color-coding and the increasing point size is identical to Figure 3. The maximum R_{FeII} value ($R_{\text{FeII}} \approx 1.552$) is recovered for a BLR density, $\log n_{\text{H}} = 12 \text{ (cm}^{-3}\text{)}$ and for the ionization parameter, $\log U = -2.0$. Note that, these conditions imply a $R_{\text{CaT}} \approx 0.282$. Similarly, for the maximum R_{CaT} (≈ 0.313), this value of density is identical as above, but for a slightly lower ionization parameter, i.e, $\log U = -2.25$, which corresponds to $R_{\text{FeII}} \approx 1.249$. The non-monotonic trends are seen for both R_{FeII} and R_{CaT} . For the given range of cloud densities, we see that the positions of the peak values for R_{CaT} per ionization parameter, shift toward lower densities, starting at $\log n_{\text{H}} = 13.0 \text{ (cm}^{-3}\text{)}$ for a $\log U = -3.25$ (although there’s only one data point for this case), going till $\log n_{\text{H}} = 11.75 \text{ (cm}^{-3}\text{)}$ for a $\log U = -1.5$. This trend is almost consistent for the R_{FeII} and the range of densities for the corresponding peak R_{FeII} values are similar to R_{CaT} .

Further increase in the density (for $\log n_{\text{H}} > 12 \text{ cm}^{-3}$) leads to a clear decline in both the R_{CaT} and R_{FeII} values. This is quite straightforward, as we have fixed the maximum column density at 10^{24} cm^{-2} , the corresponding cloud depth gradually decreases with an increase in cloud density. Hence, the total integrated intensity drops with increasing density. Although, for the densities $\log n_{\text{H}} \leq 13.0 \text{ (cm}^{-3}\text{)}$, we can observe the peak emission (for both R_{CaT} and R_{FeII}) when the cloud depth is comparable to the cloud density, i.e. $d \text{ (cm)} \sim 10^{11.75} - 10^{12.25}$ (see Figure 6).

Table 1. Physical parameters for the 58 sources

Object	z	R_{FeII}	R_{CaT}
Persson (1988) Sample			
IZw 1 [†]	0.061	1.778 ± 0.050	0.513 ± 0.130
Mrk 42	0.025	1.072 ± 0.070	0.407 ± 0.141^a

Mrk 478 [†]	0.077	0.933 ± 0.060	0.234 ± 0.070
II Zw 136	0.063	0.661 ± 0.050	0.170 ± 0.133
Mrk 231	0.044	2.455 ± 0.050	0.417 ± 0.192
3C 273	0.159	0.398 ± 0.050	0.123 ± 0.040
Mrk 6	0.019	0.832 ± 0.160	$0.468 \pm 0.431^*$
Mrk 486	0.039	0.269 ± 0.060	$0.065 \pm 0.042^*$
Mrk 1239 [†]	0.02	1.096 ± 0.070	0.110 ± 0.071^a
Mrk 766	0.013	0.676 ± 0.120	$0.309 \pm 0.249^*$
Zw 0033+45	0.047	0.525 ± 0.100	$0.155 \pm 0.079^*$
Mrk 684	0.046	1.288 ± 0.070	0.155 ± 0.103
Mrk 335 [†]	0.026	0.417^u	0.025^u
Mrk 376	0.056	0.617 ± 0.060	0.049 ± 0.030^b
Mrk 493 [†]	0.032	0.776 ± 0.060	$0.209 \pm 0.183^*$
Mrk 841	0.037	0.209^u	0.032^u
Ton 1542	0.063	0.363^u	0.05^u
VII Zw 118	0.079	0.447^u	0.076^u
Mrk 124	0.057	0.708^u	0.078^u
Mrk 9	0.04	0.398^u	0.036^u
NGC 7469	0.016	0.339^u	$0.045^{*,u}$
Akn 120	0.034	0.468^u	0.062^u
Mrk 352	0.014	0.219^u	$0.048^{*,u}$
Mrk 304	0.066	0.282^u	$0.017^{*,u}$
Mrk 509	0.034	0.129^u	0.041^u

Martínez-Aldama et al. (2015a) Sample

HE0005-2355	1.412	0.933 ± 0.237	0.166 ± 0.107
HE0035-2853	1.638	1.479 ± 0.170	0.447 ± 0.041
HE0043-2300	1.54	0.316 ± 0.044	0.214 ± 0.025
HE0048-2804	0.847	0.617 ± 0.114	0.102 ± 0.075
HE0058-3231	1.582	0.589 ± 0.176	0.389 ± 0.090
HE0203-4627	1.438	0.759 ± 0.192	0.479 ± 0.088
HE0248-3628	1.536	0.372 ± 0.034	0.251 ± 0.023
HE1349+0007	1.444	0.692 ± 0.143	0.234 ± 0.086
HE1409+0101	1.65	1.549 ± 0.107	0.316 ± 0.066
HE2147-3212	1.543	1.479 ± 0.375	0.490 ± 0.079
HE2202-2557	1.535	0.537 ± 0.062	0.117 ± 0.019
HE2340-4443	0.922	0.224 ± 0.021	0.089 ± 0.064
HE2349-3800	1.604	0.832 ± 0.057	0.288 ± 0.093
HE2352-4010	1.58	0.447 ± 0.031	0.170 ± 0.023

Martínez-Aldama et al. (2015b) Sample

HE0349-5249	1.541	1.704 ± 0.102	0.165 ± 0.014
HE0359-3959	1.521	1.173 ± 0.070	0.371 ± 0.031
HE0436-3709	1.445	1.164 ± 0.070	0.335 ± 0.028
HE0507-3236	1.577	0.291 ± 0.006	0.119 ± 0.034
HE0512-3329	1.587	0.810 ± 0.017	0.240 ± 0.050
HE0926-0201	1.682	1.139 ± 0.082	0.374 ± 0.033
HE1039-0724	1.458	0.289 ± 0.021	0.033 ± 0.018
HE1120+0154	1.472	0.204 ± 0.012	0.084 ± 0.011

Marinello et al. (2016) Sample			
1H 1934-063	0.011	1.404 ± 0.223	0.368 ± 0.047
1H 2107-097	0.027	1.047 ± 0.106	0.139 ± 0.019
IZw 1 [†]	0.061	2.286 ± 0.199	0.564 ± 0.058
Mrk 1044	0.016	1.181 ± 0.127	0.111 ± 0.016
Mrk 1239 [†]	0.019	1.340 ± 0.147	0.148 ± 0.016
Mrk 335 [†]	0.026	0.818 ± 0.092	0.054 ± 0.007
Mrk 478 [†]	0.078	1.023 ± 0.089	0.514 ± 0.056
Mrk 493 [†]	0.032	1.721 ± 0.179	0.387 ± 0.046
PG 1448+273	0.065	1.189 ± 0.129	0.262 ± 0.034
Tons 180	0.062	0.985 ± 0.110	0.145 ± 0.015
Marinello et al. (2020)			
PHL 1092	0.394	2.576 ± 0.108	0.839 ± 0.038

NOTES. Columns are as follows: (1) Object name. (2) Redshift. (3) $R_{\text{FeII}} = \text{EW}(\text{FeII}_{4434-4684})/\text{EW}(\text{H}\beta)$. (4) $\text{CaT} = \text{EW}(\text{CaT})/\text{EW}(\text{H}\beta)$. In column 1 ([†]) symbol represents the 5 common sources in Persson (1988) and Marinello et al. (2016) samples. In column 4, * symbol indicates sources with a possible host galaxy contribution in the CaT emission lines, *a* letter indicates the presence of a central dip in the CaII emission lines, *b* letter marks a questionable CaT detection, and *u* letter indicates an upper limit in H β and CaT intensity.